8-1-2018

Time reversal symmetry breaking in 4f-doped Topological Insulators

Stephen Hofer
Southern Illinois University Carbondale, shofer@siu.edu

TIME REVERSAL SYMMETRY BREAKING IN 4F-DOPED TOPOLOGICAL INSULATORS

by

Stephen Hofer

B.S., Southern Illinois University, 2010

A Thesis
Submitted in Partial Fulfillment of the Requirements for the
Master of Science Degree

Department of Physics
in the Graduate School
Southern Illinois University Carbondale
August, 2018

THESIS APPROVAL

TIME REVERSAL SYMMETRY BREAKING IN 4F-DOPED TOPOLOGICAL INSULATORS

By

Stephen Hofer

A Thesis Submitted in Partial

Fulfillment of the Requirements

for the Degree of

Master of Science

in the field of Physics

Approved by:

Dr. Dipanjan Mazumdar, Chair

Dr. Thushari Jayasekera

Dr. Naushad Ali

Graduate School
Southern Illinois University Carbondale
June 29, 2018

AN ABSTRACT OF THE THESIS OF

Stephen Hofer, for the Master of Science degree in Physics, presented on June 29, 2018, at Southern Illinois University Carbondale.

TITLE: TIME REVERSAL SYMMETRY BREAKING IN 4F-DOPED TOPOLOGICAL INSULATORS

MAJOR PROFESSOR: Dr. Dipanjan Mazumdar

Time-Reversal Symmetry (TRS) is a hallmark of Topological Insulator (TI) systems. TRS in conjuction with the strong Spin-Orbit Coupling (SOC) present in Bismuth Selenide is responsible for the uniquely robust surface states shown in this material. Breaking TRS in these systems in order to achieve gapped surface states requires the presence of a magnetic field throughout the material. We achieve this effect by doping the system with 4f elements whereby the magnetic field is provided by the local magnetic moments of the dopants manifesting ferromagnetic behavior. Through this spontaneous gap opening in the surface states in is expected that the Quantum Anomalous Hall Effect is present in the system.

This thesis provides experimental evidence of good candidate materials for measuring the Quantum Anomalous Hall Effect. By combining X-ray Diffraction to ensure good crystal growth, Angle-resolved Photoemission Spectroscopy probe to the evolution of the bandstructure as an effect of doping and Density Functional Theory to support the experimental data it is shown in this work that Samarium doped Bismuth Selenide is a prime candidate for displaying the Quantum Anomalous Hall Effect.

DEDICATION

Dedicated to my parents...

ACKNOWLEDGMENTS

I would like to thank my advisor, Dr. Dipanjan Mazumdar, for giving me the guidance and freedom to pursue the ideas that became this thesis. I would also like the thank Dr. Mazumdar for his work in making the connections necessary to take my research to other universities and national laboratories. In particular I would like to thank Dr. Guang Bian and Qiangsheng Lu of Missouri Univeristy at Columbia for their work in the ARPES measurements. I would also like to thank Dr. Jessica McChesney for her help in Resonant ARPES experiments at Argonne National Laboratory. Additionally I would like to recognize the faculty of the Southern Illinois University Physics Department for their work in furthering my education. In particular I would like to thank Dr. Kuloth Shajesh, Dr. Leo Silbert, Dr. Eric Chitambar and Dr. Thushari Jayasekera whose courses broadened my knowledge of physics and encouraged me to become a more proficient problem solver. I would also like to thank Dr. Naushad Ali for access to his laboratory and Dr. Igor Dubenko, Anil Aryal and Supid Pandey for their help performing SQUID experiments.

I would also like to thank my labmates and classmates for their help and camaraderie. Much appreciation to my labmates Yub Raj Sapkota, Hassana Samassekou, Asma Alkabsh and Said Bakkar for their patience, encouragement and honesty while listening to every idea that I came up with.

Lastly, but not least, I would like to thank my family and friends for their unconditional support and for helping me to keep perspective. Special thanks to my mother who has always encouraged me and never hesitated to do anything to help me achieve my goals.

PREFACE

Topological Insulators are quantum materials which are characterized by the topological nature of their electronic bandstructure. Most simply, these materials exhibit the behavior of having gapped electronic states in the bulk of the material, while showing metallic electronic behavior on the surface. This phenomenon can be explained by classifying the topology of the electronic bandstructure of the bulk as different than that of the vacuum with the surface of the material acting as the boundary between the material and the vacuum. It is very easy to see that the topology of the vacuum is trivial, which indicates that if the insulating bulk has a non-trivial topology then the phase transition between the non-trivial bulk and the trivial vacuum should produce states that pass through the Fermi energy and manifest themselves as metallic electronic states at the surface. The origin of this non-trivial topology in the bulk and its consequences will be discussed in further sections.

TABLE OF CONTENTS

LIST OF FIGURES

CHAPTER 1

BACKGROUND

1.1 HALL EFFECT

While the connection of topology to a materials surface conductivity was discovered fairly recently, the study of conduction along the boundaries of a material dates back to 1879 with the Hall effect.[1] The Hall Effect is a result of the Lorentz force acting on electrons moving through a conductor.

$$\vec{F} = q\vec{E} + \vec{v} \times \vec{B} \tag{1.1}$$

From the schematic Figure 1.1 we see that as electrons move through the material longitudinally they feel a transverse force due to the applied magnetic flux through the material. After some time the system settles into a steady-state arrangement and a transverse voltage is produced which we call the Hall Voltage (V_h). From V_h we can determine a transverse conductance σ_{xy}. Taking this experiment further and applying a magnetic field to two dimensional material gives another interesting result. [2]

Now that the electrons are confined to their local nucleus they undergo cyclotron motion as shown in Figure 1.2 . In the interior the electrons remain bound to the parent nucleus and remain insulating. The electrons on the edges of the material cannot complete

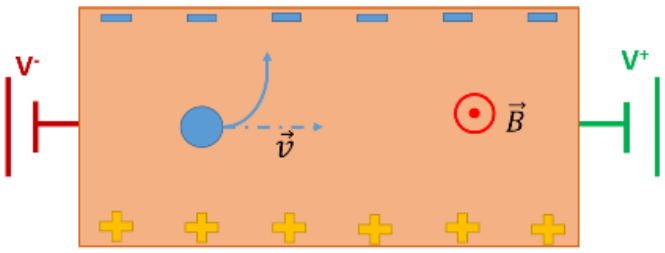

Figure 1.1. Schematic of Hall effect geometry.

a full rotation as they get reflected by the potential difference from the lattice and vacuum boundary and therefore must hop to the neighboring nucleus, inducing a current on the edge of the material. Using solutions of the harmonic insulator in conjunction with the Landau gauge we can determine that this current and therefore the transverse conductivity is quantized in units of $\frac{e^2}{h}$ which undergo transitions as the magnetic flux B is increased. This phenomenon is known as the Integer Hall Effect (IHE). These transitions occur as the Landau levels are tuned and pass through the Fermi Energy. This effect can also be achieved by gating the device and tuning the Fermi Energy (or Chemical potential) into static Landau levels, keeping the magnetic field constant. [3]

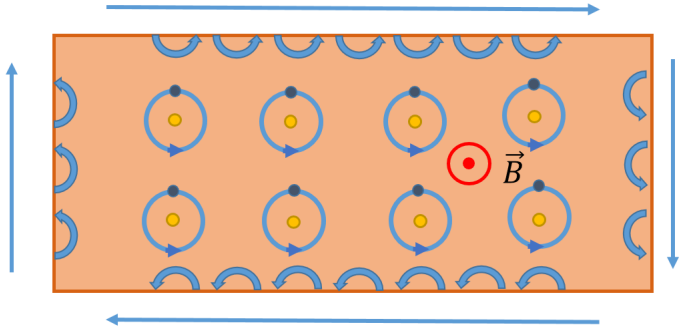

Figure 1.2. Edge current in the absence of an applied electric field.

1.1.1 Integer Quantum Hall Effect

The IHE can be seen in two dimensional systems such as 2DEGs, and recently graphene or monolayers of other gapped layered materials.[4] An interesting consequence of these transitions of the transverse conductivity is the vanishing of the longitudinal resistivity. At first glance this may seem that the material should be superconducting in this direction, however, when treating the conductivity and resistivity as elements of a matrix we see that when the longitudinal resistivity vanishes the longitudinal conductivity vanishes as well.

This IHE, also called the Quantum Hall Effect, was first theorized by Ando,

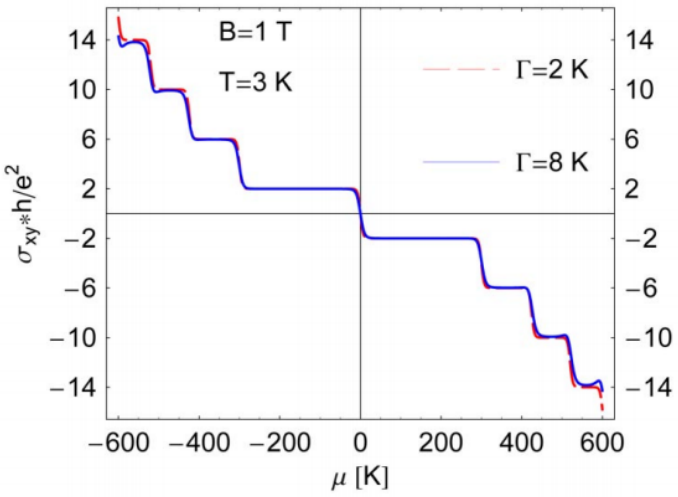

Figure 1.3. Integer Quantum Hall Effect taken from [4]. Γ indicates the width of the Landau Levels in this case.

Matsumoto and Uemura in 1974[5] and experimentally verified in 1980 by von Klitzing[6], for which von Klitzing won the 1985 Nobel Prize in Physics (see figure 1.3. It is in this theory where the first connection of electronic behavior was first connected to topology by relating the integer ν to the first Chern numbers, which are closely related to Berrys phase. In the spirit of keeping the narrative on track an explanation of Berrys phase and its importance to the topology of electronic bandstructure will be discussed in a future section.

There are, however, ways to produce systems which display these effects without applying an external magnetic flux. If, for example, the system contains a ferromagnetic order the Hall Effect and Quantum Hall Effect can be observed without supplying a magnetic flux, which we refer to as the Anomalous Hall Effect and Quantum Anomalous Hall Effect.[7] Systems displaying the QAHE are sometimes referred to as Chern Insulators.[8]

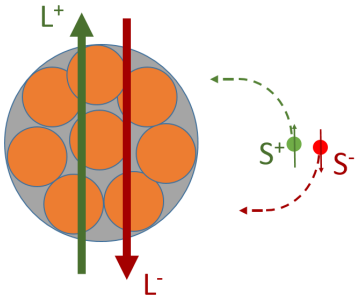

Figure 1.4. Interaction of electron spin-angular momentum S, and orbital-angular momentum L.

1.2 SPIN-ORBIT EFFECTS

So far in our discussion of the Integer Quantum Hall Effect we have ignored the role of spin and special relativity in electron behavior. Specifically, how does an electrons motion around its parent nucleus interact with the electric field produced by the protons which rest in the nucleus? We know from relativity that a charged particle under the influence of an electric field will behave as though some of the field is magnetic flux if the electron is moving at relativistic speeds. Then the question becomes, under what conditions does and electron in a crystal lattice meet these requirements? A simplistic approach is to treat electron orbitals classically at first, with some requirements about their behavior that we know from quantum mechanics. We know a few things about orbital mechanics from Keplers law, which relates the period of an orbit to the charges of the satellite and central charge as well as the distance of the orbit from the central charges. This suggests that for any given distance of the orbit of an electron, as the central charge increases then the period of oscillation will decrease and the electron must move faster to maintain a stable orbital. In this case the central charge is determined by Z, which is the number of protons in the nucleus, which determines the element in question. This effect of electrons behaving as though the nucleus is producing a magnetic field is most easily seen in high Z elements such as Hg, Te, and Bi. By including high Z elements in the system the Hall Effect can be realized without supplying a magnetic flux

or ferromagnetic order.

1.3 TIME REVERSAL SYMMETRY

If we consider the orbital angular momentum of the electron producing a relativistic magnetic field, then we must also consider its spin angular momentum and its interaction with the resulting field. In order to minimize the interaction energy between the spin and orbital angular momentum the electron will now have a preferred direction of motion dependent on its spin orientation.

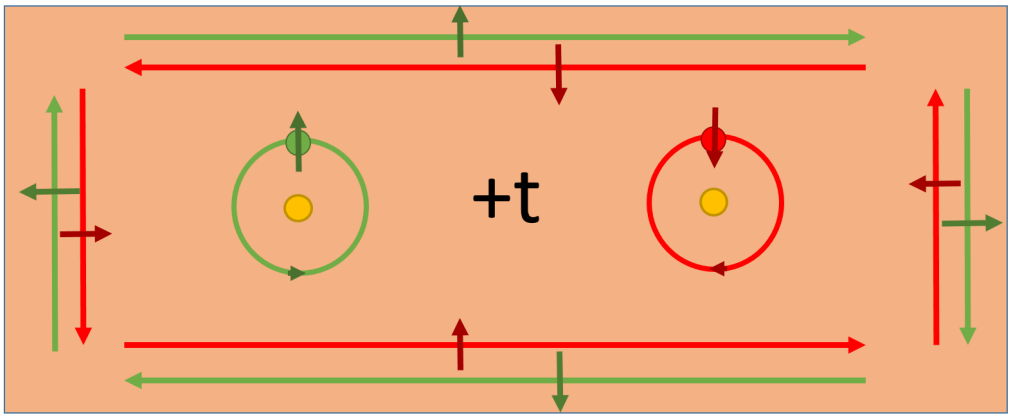

Figure 1.5. Spin current induced by spin-orbit coupling.

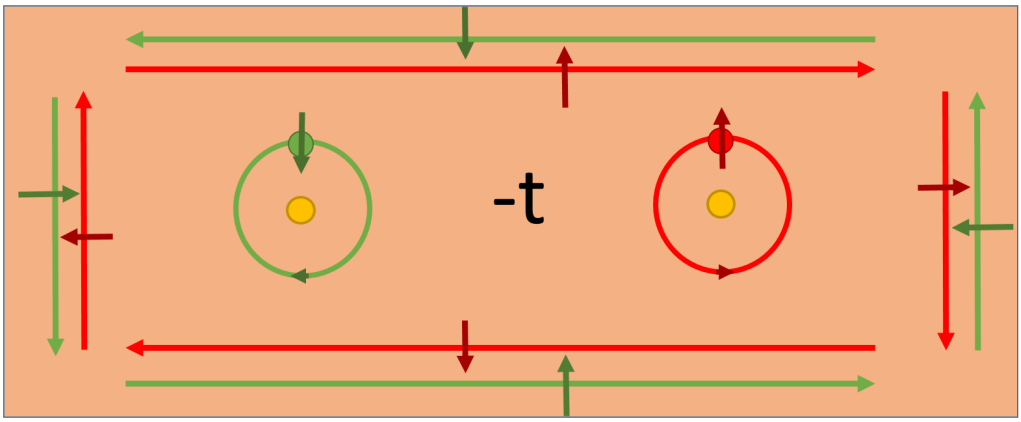

Figure 1.6. Time-reversed spin-orbit coupling. Spin current flow remains unchanged.

In two dimensional systems this manifests as two opposing spin current edge states where no electric charge is transferred. This system displays Time-Reversal symmetry (TRS) which a hallmark of Topological Surface States (TSS). In three dimensional systems these two dimensional surface states are subject to spin-momentum locking, where the spin of an electron and its momentum vector are interlocked, which produces a non-trivial spin texture in momentum space. These three dimensional systems displaying TRS and TSS are what we call Topological Insulators and were first discovered in 2008 by David Hsieh at Princeton[9].

The result of Spin-Orbit coupling is a very robust Spin-Momentum locking effect, wherein the Spin direction of the electron is uniquely tied to its momentum vector. Within the bulk bandgap the surface states take on a unique spin texture in the momentum space. These helical spin-textures can be mapped onto the unit sphere, where they can be seen to be topologically non-trivial skyrmion charges.

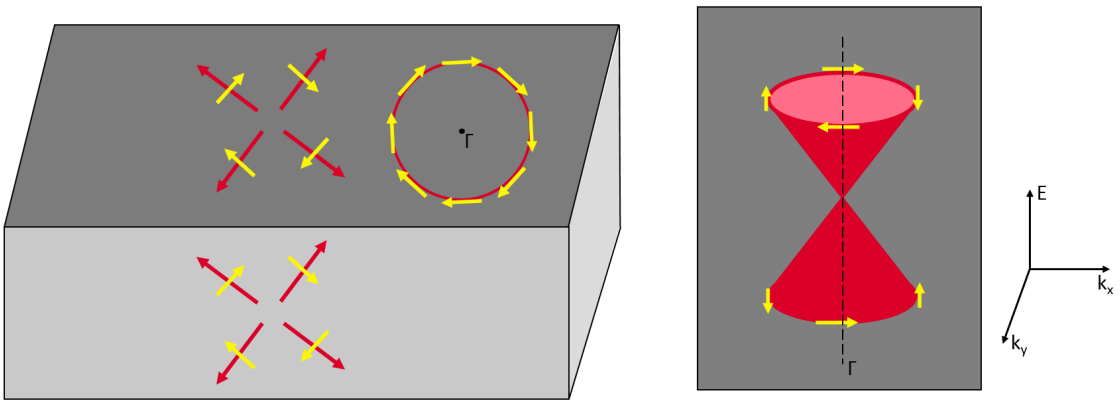

Figure 1.7. Spin texture on the surface of a 3-dimensional TI. Spins become degenerate at the Dirac Point.

Above and below the Dirac point the surface states change their helicity, owing to the change in mass sign above and below the Fermi energy, a consequence of the band inversion.

To better understand the effect of topology on electronic bandstructure, we must

move to a discussion of what do we mean by topology in the context of the Hamiltonian of the system and how its eigenvalues are affected by various physical phenomena. Topology can be used to classify different systems as belonging to the similar or disimilar groups. If two systems have the same topology then one of these systems can be moved adiabatically to the other system, and vis a versa. In the study of Hamiltonians we can classify groups of Hamiltonians by how many electronic states they have below the Fermi Energy, which we will call the Topological Invariant Q. This means that any Hamiltonian with TI of Q=2 is topologically to any other Hamiltonian with Q=2. Let us then consider the case where we take a Hamiltonian H_1 with Q=1 and attempt to transform it to a hamiltonian H_2 with Q=2.

$$\tilde{H} = H_1(1-\alpha) + H_2(\alpha) \tag{1.2}$$

Here our parameter alpha controls the contributing of H_1 and H_2 on the total Hamiltonian $\tilde{H}$. We can see that if our original definition of Q holds, then at some value of α the topological class of $\tilde{H}$ will transition from Q=1 to Q=2. We call this a topological phase transition and it is characterized by the energy eigenvalue of an electronic state crossing the Fermi Energy. This explanation holds up well for zero dimensional quantum dots but we would like to extend this idea of topology to higher dimensions.

In one dimension it is useful to use the Su-Schrieffer-Heeger model(Figure 1.8). Using a tight-binding model we can build a Hamiltonian of some one dimensional chain of lattice points whose eigenvalues are parameterized by the hopping parameters v and u.[10]

$$H = \sum_{a,b} [v c_a^\dagger c_b + u c_b^\dagger c_a + h.c.] \tag{1.3}$$

Using Bloch's Theorem to force periodicity into the solutions of the Hamiltonian we obtain

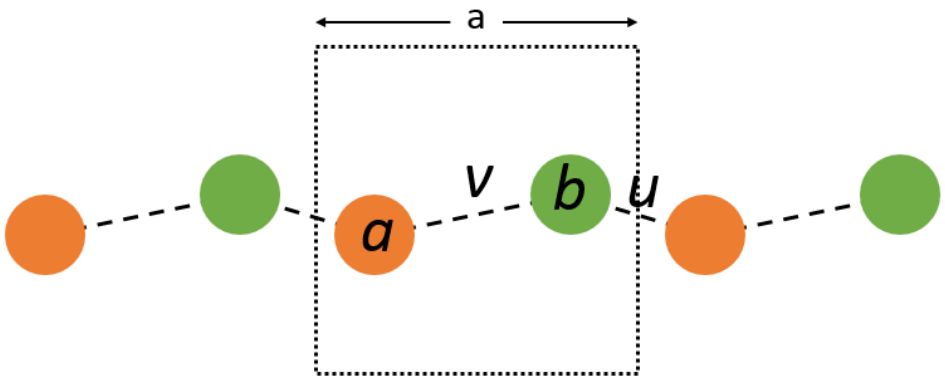

Figure 1.8. Model of Poly-acetylene, a 1-D chain of Carbon atoms. Hydrogen bonds not shown.

$$\tilde{H} = \sum_{a,b} [h_{a,b}(v + ue^{ika})] \tag{1.4}$$

Since this Hamiltonian describes a two particle system due to the contribution of one electron from each carbon sublattice our $h_{a,b}$ matrix is two by two and can be expressed in terms of the pauli matrices.

$$h_{ab} = d_0 \otimes 1 + \sum_i [d(\vec{k}) \otimes \sigma_i] \tag{1.5}$$

where $d_0 = 0$, $d_x = v + ucos(ka)$, $d_y = usin(ka)$ and $d_z = 0$

Above we see as the relationship between v and u changes our system goes through various transitions. We can define a topological invariant for these one dimensional systems as the winding number, or how many times the vector $d(\vec{k})$ encircles the origin. This winding number is closely related to Berry's phase[11] where Berry's phase is given by $\gamma = \nu\pi$. We can see that a topological phase transition occurs between $v > u$ where ν=0 and $v < u$ where ν=1. We call ν=0 topologically trivial and ν=1 topologically non-trivial. Another interesting feature of this topological phase transition is that the

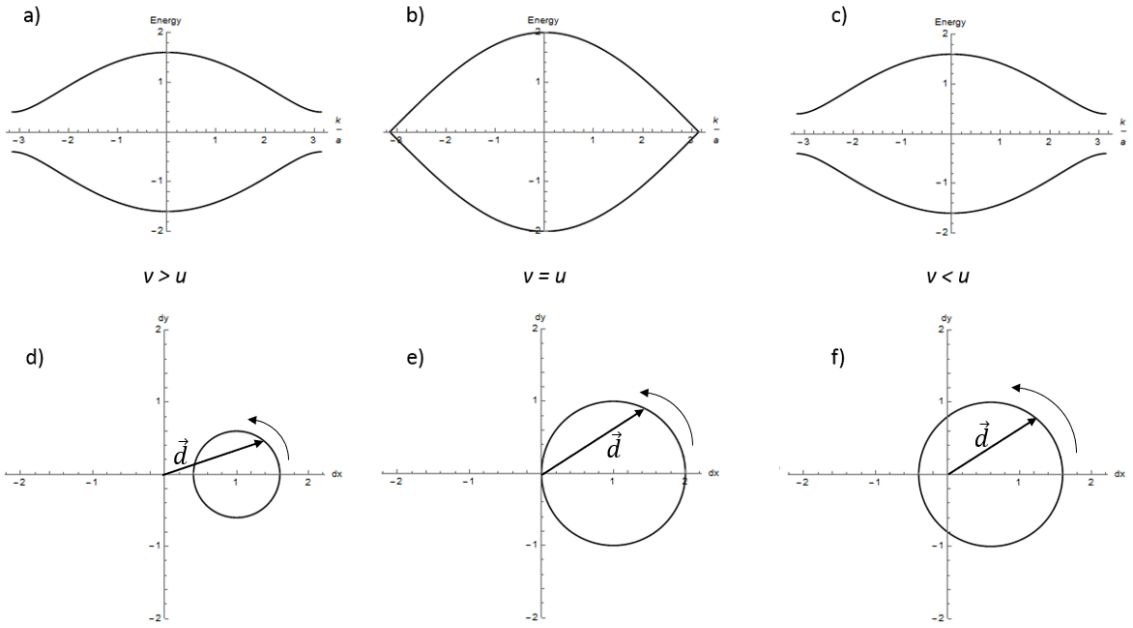

Figure 1.9. (a),(b),(c): Energy dispersion at different v,u inequalities. (d),(e),(f): Tracing out the path of $d(\vec{k})$ in parameter space.

band dispersion for $v > u$ and $v < u$ are practically identical insulating phases. The point of the phase transition occurs at $v = u$ where the bands close their gap and become conducting. This feature was seen in the one dimensional quantum dot case where an electron passed through the Fermi Energy and switched between the valence and conduction bands. This process is known as band inversion and can occur due to a number of effects.

In two dimensional systems CdTe-HgTe-CdTe heterostructures[12] are the model example. The bandstructure of CdTe and HgTe near the Γ point are quite similar. In CdTe the Γ_6 s orbital and Γ_8 p orbital are above and below the fermi energy, respectively. In HgTe the opposite is true. By creating a heterostructure of these materials the band characteristics of at the interface of these layers depends on the mixing of the eigenstates of both systems. At some critical thickness of the HgTe layer, the mass parameter is equal to zero, indicating and change in sign. Above and below this critical thickness the bands look similar, although inverted, and is characterized by an energy gap dependent

on the value of the mass parameter. What is not similar is the number of pairs of edge states. In this case, where time-reversal symmetry is present in the Hamiltonian, each eigenvalue is two-fold degenerate due to the equivalent spin-up and spin-down eigenvalues. This is a consequence of Kramers degeneracy and these pairs are called Kramers pairs. By counting the number of Kramers pairs in the edge states of our system we see that the topologically non-trivial state is characterized by an odd number of Kramers pairs, and the topologically trivial state is characterized by an even number of Kramers pairs. With this information it is easy to decide on a topological invariant for these two-dimensional systems by determining if the number of edge states is odd or even. The easiest way to determine this is to take the number of edge states, modulo 2. This is known as the Z_2 invariant[13] which outputs a value of +1 (even) or -1 (odd). The Quantum Spin Hall state occurs when the Z_2 invariant is 1, and the typical Charge Hall state occurs for values of Z_2= +1. These two states are mutually exclusive due to the presence or breaking of time-reversal symmetry.

$$Z_2 = (-1)^{\nu} \tag{1.6}$$

In the three dimensional regime the major contributor to band inversion is Spin-Orbit coupling. For this reason the only strong three dimensional TIs are compounds with heavy elements, typically Bi, Te, Pb, Hg, Pt, etc. In order to undergo the band inversion, the Spin-Orbit energy shift (Δ_{so}) should be greater than the non-relativistic bandgap. For example, despite having similar chemistry, Sb2Se3 is not a strong TI, where as $(Bi_xSb_{1-x})_2Se_3$ is. At a critical value of x the Spin-Orbit shift in the energy eigenvalues overcomes the non-relativistic bandgap and the band inversion occurs. We also deal with the topological Z2 number similarly to the 2D case, however we need to now consider the full three dimensional brillouin zone. To fully describe the topology of the system we need 4 topological numbers. The first and most important is the strong Z_2 invariant, which runs across all 8 Time-Reversal Invariant Momenta at the corners of the

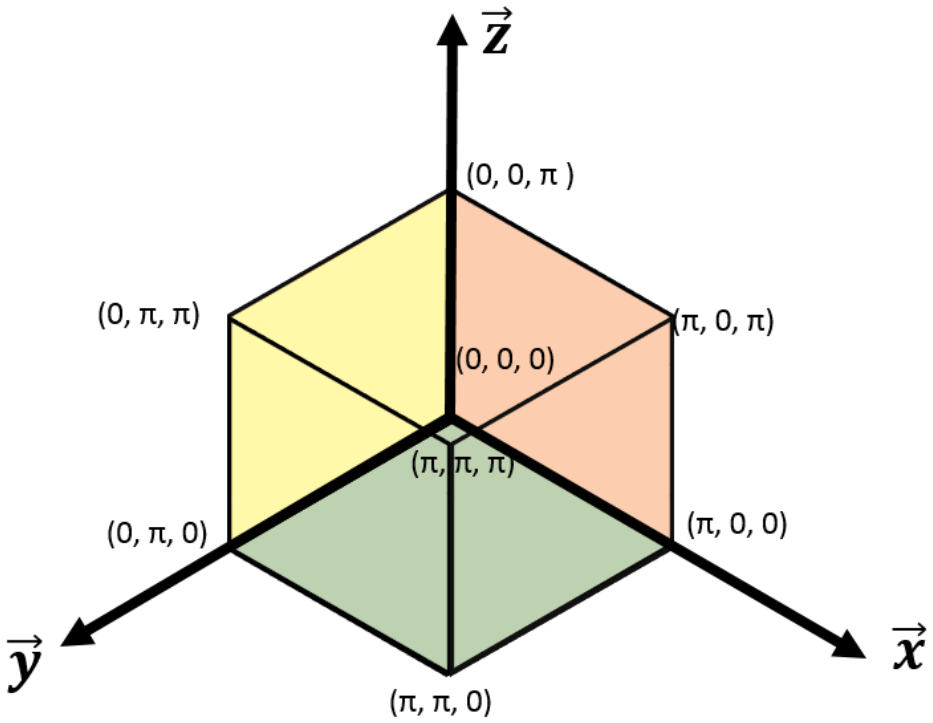

Figure 1.10. Generalized Brillouin zone with TRIMs.

three dimensional brillouin zone as shown in figure 1.10. The other 3, known as the weak invariants, run across the corners of the xy, yz, and zx planes, starting from Γ. The weak invariants are identical to the 2D case if the system is reduced to that dimension.

Although TRS is present in these systems, other similar systems where TRS is spontaneous broken can lead to novel states of matter.[7, 14] The Quantum Anomalous Hall State can be achieved by inducing a spontaneous ferromagnetic ordering to the system by either doping or proximity effects in grown heterostructures. [15–23] Ferromagnetic insulators are another state which must undergo TRS breaking. Non-typical superconducting states can also theoretically be achieved with TRS broken topological states, as well as searching for exotic particles. [24–30]

CHAPTER 2

CONTEXT AND HYPOTHESIS

In this chapter we will discuss the current state of research to provide the context for this work as well a motivation for the hypothesis presented.

2.1 TOPOLOGICAL INSULATORS

As stated previously, 3D Topological Insulators were experimentally verified in 2008, with many more soon following in 2009.[9][31][32] $Bi_{0.9}Sb_{0.1}$ was the first material measured with ARPES to directly map the TSS. In this compound the band inversion occurs at the L point in the Brillouin zone when the compound is doped to $Bi_{0.96}Sb_{0.04}$. At this particular doping the bandstructure gives rise to a massless Dirac point. Beyond this doping the compound becomes an inverted-band insulator whose low-energy physics near the L point are dominated by the spin-orbit interaction.

In figure 2.1 we can see the ARPES data taken by Hsieh on the system $Bi_{0.9}Sb_{0.1}$. The L point measured was in the third Brillouin zone at coordinates $(k_x, k_y, k_z) =$ (0.8,0,2.9)Å^{-1}. In the k_y direction we see a linear relationship between $\vec{k}$ and Energy, suggesting a massless Dirac particle in this direction. A much more complicated parabolic and indirect bandstructure is shown in the k_x direction, owing to the effects of spin-orbit interaction in the band inversion.

Later, in 2009, an experimental study of the bandstructure of Bi_2Te_3 was published in Science by Y.L. Chen et. al. In figure 2.2 the TSS (Surface State Bands in the figure) are present within the Bulk bandgap. In this material the band inversion occurs at the Γ point. By convention the three dimensional Brillouin zone is projected onto the two dimensional Brillouin zone when doing theoretical bandstrucutre analysis. Therefore the path $K \rightarrow \Gamma \rightarrow M$ is typically used for rhombohedral structures with inversion at the Γ point. The reason for this is due to the surface sensitivty of ARPES, which results in data that is best represented in two dimensions. The k_z dispersion can be measured by

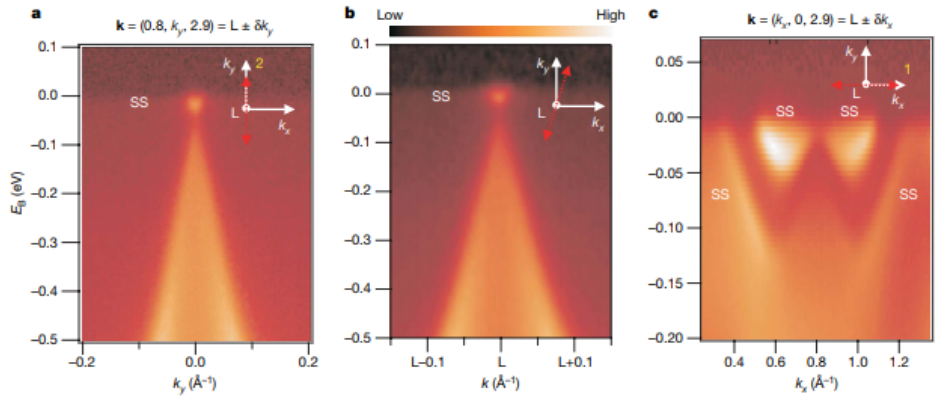

Figure 2.1. ARPES data of $Bi_{0.9}Sb_{0.1}$ centered around L along the k_y, intermediate, and k_x directions, respectively. Taken from [9].

measuring across multiple Energy values. Although there should be zero dispersion in the k_z direction, sometimes it is mapped to verify this.

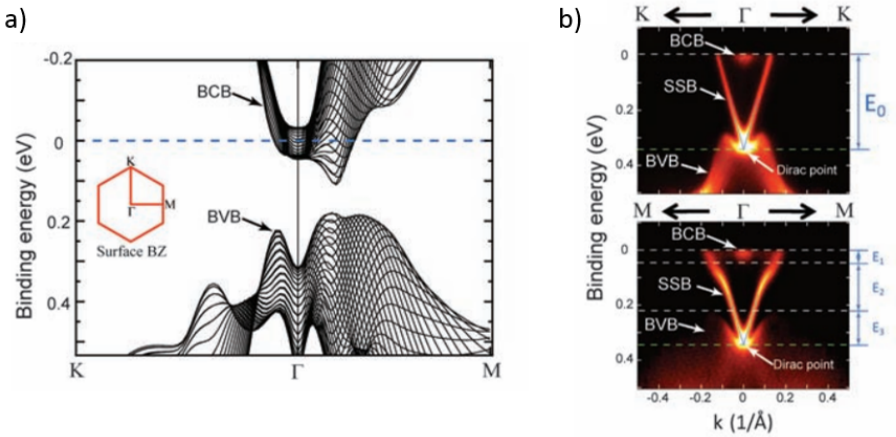

Figure 2.2. Bi2Te3 Arpes and Theory. Taken from [31].

In this measurement we can see the Dirac point occurs below the Valence Band Maximum. It was also noted in this work that doping the Bi sites is important in reducing the carrier concentration to achieve a true insulating state. Due to Te vacancies and anti-site defects, the stoichiometric material tends to be n-type, thereby raising E_f into the conduction band. By doping with Sn the carrier concentration was reduced, tuning E_f into the bulk bandgap and achieving a true Topological Insulator.

The Topological bandstrucutre of Bi_2Se_3, which is the focus of this work, was also reported experimentally in 2009 by Xia et. al. Bi_2Se_3 has a similar bandstructure to Bi_2Se_3, unsurprisingly. It's band inversion is spin-orbit induced at Γ as well as having an indirect Bulk bandgap near Γ also as a consequence of spin-orbit coupling. Worth noting is the correspondence of the $K \to \Gamma \to K$ and $M \to \Gamma \to M$ ARPES data to the $K \to \Gamma \to M$ theoretical calculation. In practice, isolating the k_z reciprocal vector is trivial, as this family of materials tends to cleave along its basal plane, exposing the surface normal to the k_z vector. However in order to get precise measurements along the k_x or k_y directions one must know the in-plane orientation of the crystal. One effective method is Laue diffraction to map the reciprocal lattice, but this must be done in-situ and is not always feasible for all experimental set-ups.

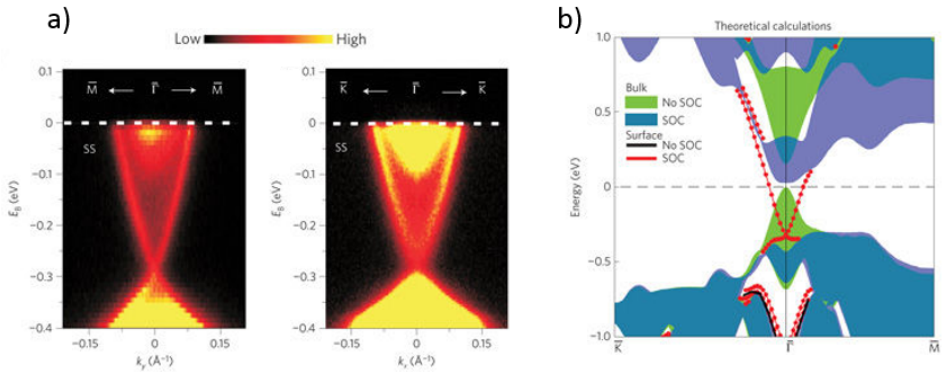

Figure 2.3. Bi2Se3 ARPES and Theory. Taken from [32].

2.2 MAGNETIC DOPING

Because of the exotic properties promised by breaking TRS in TIs[14, 15, 29] much work has also been done in doping these systems to achieve this goal. Transition metals were, of course, the first systems believed to be able to achieve this effect. Elements such as Cr, Mn, Fe and Co were doped into TI systems to varying degree of success. Rare-earth elements have also been doped in these systems to explore magnetic ordering.

[15–17, 33–39]

Due to the spin degeneracy imposed by normal TRS in undoped TIs, the Anomalous Hall Effect in these systems transports spin, instead of charge. However, when magnetic impurities are introduced into the system, the Hall Effect transports charge, due to the spin-polarization present in the magnetic ordering. Therefore it is of greatest interest to measure the QAHE in these magnetically doped systems. [15–21, 36] These systems require tuning the chemical potential of the material into the gap of the surface states to measure the QAHE. The location of E_f in the energy spectrum due to doping and vacancies is paramount in determining if attempting to measure the QAHE is feasible in the system. ARPES is a useful tool in determining sample candidates which are viable in their ability to display the QAHE. To this end much work has been done on the 3d transition metal dopants [33, 35, 39], however, at the time of this writing, comparatively little work has been done to characterize the nature of Rare-earth dopants through ARPES.[40–43]

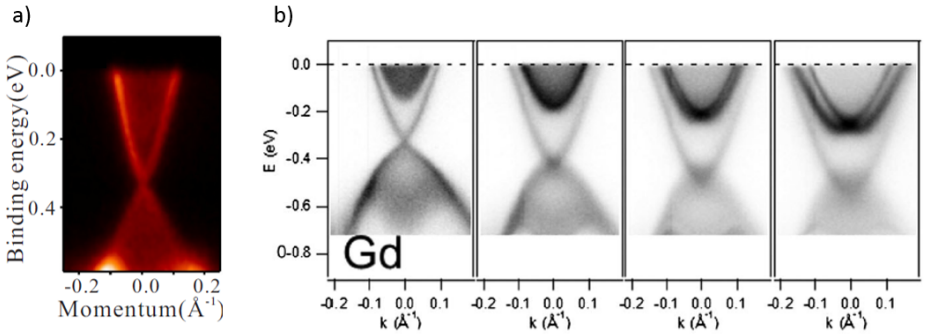

Figure 2.4. Gd doped ARPES from [40],[41] respectively.

The main obstacle in 3d doping of Bi_2Se_3 in particular seems to be a mismatch of the atomic size of the dopant and Bismuth. Because of this the 3d dopant may occupy Bi sites as well as undesirable interstitial sites. This could give rise to competing magnetic orderings within the material, thereby lowering the magnetic transition temperatures.

[44, 45] Rare-earth Lanthanides, however, have relatively large ionic radii which are very close in value to Bismuth, thereby restricting the sites which they can occupy and promoting a single magnetic ordering in the system. Additionally rare-earth elements tend to have much higher magnetic moments than their transition metal counterparts.

2.2.1 Hypothesis

For these reasons this work has focused on the synthesis and characterization of Gd and Sm doped Bi_2Se_3. It is then expected that with enough Gd doping the system will form an AFM phase with a $T_N < 10$K. The result of this will be that TRS will be broken locally at the impurity sites, but the metallic TSS should be conserved throughout the material. Also, due to the unique topological spin-texture present in the system, this AFM phase may show novel long-range order. In the Sm doped sample it is expected that a FM phase will form with a T_C near 50K, breaking TRS throughout the system and thereby inducing a gap in the TSS. A consequence of this would be the formation of a QAHE state in the system, which will require more thorough investigation.

CHAPTER 3

METHODS

3.1 GROWTH

All materials were grown in evacuated quartz ampules. Ingredients were measured out in stoichiometric ratios and transferred to an unsealed tube. This tube was then attached to a vacuum system, flushed with argon and evacuated to a pressure of 10^{-6} Torr. The evacuated tube was then transferred to a furnace. The heating program then slowly heated the tube to 500°C at a rate of 1°C per minute. The temperature was kept at 500°C for 24hr and then increased to 850°C again at a rate of 1°C per minute. The temperature was then kept at 850°C for 5 days and then cooled to 600°C and was kept there for another 4 days. The ampule was then carefully removed from the furnace and quenched in water before the crystal was removed from the ampule.

3.2 X-RAY DIFFRACTION

The major technique used to characterize the crystallininty of the prepared samples was X-ray Diffraction. In this section we will discuss the theory behind X-ray Diffraction as well as the experimental effects one must consider to measure a sample.

3.2.1 Theoretical Background

The basic idea of X-ray diffraction is using Braggs law to measure interplanar distances in the crystal structure.

$$n\lambda = 2dsin\theta \tag{3.1}$$

However, this is a simplistic model and not very useful for in-depth analysis of the total structure. By their nature crystals are periodic and can be described by periodic functions in real space. Building a mathematical expression for the lattice structure we

can use a series of Dirac Deltas to roughly describe the crystal.

$$f = \sum_i A_i \delta(\vec{x} - \vec{x_i}) \tag{3.2}$$

Taking advantage of this fact we can express this as a series of plane-wave in reciprocal space using a Fourier Transform.

$$F = \int_{-\infty}^{\infty} f e^{i2\pi(\vec{k}\cdot\vec{x})} dx = \sum_i A_i e^{i2\pi(\vec{k}\cdot\vec{x_i})} \tag{3.3}$$

This result is known as the structure factor and will determine what allowed of (hkl) are allowed due to the symmetries present in the structure. In reciprocal space Bragg's Law becomes to Laue condition.

$$2\tilde{\mathbf{k}} \cdot \tilde{\mathbf{S}} = S^2 \tag{3.4}$$

In this way, by evaluating the reciprocal lattice at certain planes described by (hkl) we can determine the spatial frequency at which these planes occur in real space, thereby determining the interplanar distance. In experiment the effect of diffraction is to do essentially that, applying the Fourier Transform to the object through which the light diffracts. The output pattern from an X-ray Diffraction scan is then simply the spatial frequencies of the planes present in the crystal under study. In general this then explains the positions of the peaks in the diffraction pattern, but does not give information on their intensity.

To understand the way the X-rays scatter from the crystal sites we must consider their electrical nature. When the X-ray enters the material primarily what it will interact with is the electron density. Since the sourced X-rays in this case are 8keV, many of the electrons it interacts with will be emitted as photoelectrons. If instead the X-ray interacts with a core electron whose binding energy is sufficient to prevent photoemission then the X-ray will be re-emitted. If we consider the core electrons states like a hydrogenic atom,

then it is easy to see that high atomic number elements will have many more electrons that meet these requirements than lighter, low atomic number elements. In this way the peak intensities are dependent on the Z-number of the element present at the scattering site, and therefore peaks corresponding to reflections off high Z elements will appear larger. An important connection here is the relation of X-ray Diffraction to Density Functional Theory, which will be discussed in a later section. Density Functional Theory utilizes self consistent calculations of the electron density to determine the ground state wave functions of the many-electron problem. To do this, however, we must determine the background potential from the nuclei in the crystal structure which is generated by assuming the nuclei sit at the center of the high-scattering points of our electron density.

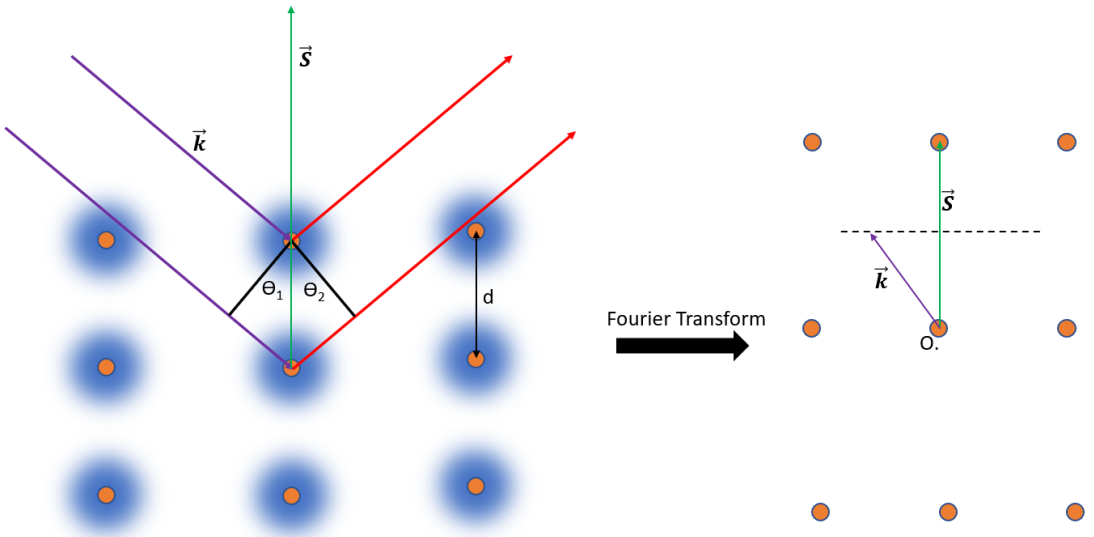

Figure 3.1. Visual representation of Bragg's Law, left, and the Laue Condition, right.

Another important factor in determining peak intensity is the multiplicity of the reflection. For example, in high symmetry crystals, such as the simple cubic, many unique planes will have the exact same interplanar distances. The (hkl) = (100) plane for example shares peak position with the planes (0 1 0),(0 0 1),(-1 0 0), (0 -1 0), and (0 0 -1) giving this peak a multiplicity of 6, since 6 unique values of (hkl) occupy the same peak

position. Other lower symmetry crystal configurations can interfere destructively, thereby reducing the expected peak intensity, particularly if the crystal is described by additional atom basis whose sites are occupied by dissimilar elements (and therefore scattering factors).

By determining the peak positions and peak intensities and comparing to known values for the parent material we can determine, roughly, what is happening to the parent compound when it is being doped. If, for example, a shift occurs in the peak positions then we can know how the dopant is altering the interplanar distances of the parent compound, and therefore the overall lattice parameters. Peak intensity can also, in theory, give information about the occupation sites of the dopant, but in practice this is difficult to accomplish, since peak intensity is also determined by many other factors. The temperature of the sample is also important in understanding both the intensity and the shape of the diffraction peak. If we treat the nuclei of the crystal as classical particles we can extract an average kinetic energy of the nuclei based on its temperature by the equation $E = k_b T$ where k_b is the Boltzmann constant. Combining this with a 3-dimensional version of the Lennard-Jones potential we can determine a range from which a nucleus can deviate from its lattice point, thereby changing the results of the crystal structure from a fixed dirac delta to a gaussian centered around the lattice point. This factor is known as the Debye Temperature factor.

Another factor in determining the peak intensity of the Lorentz-Polarization factor. The L-P factor arises when the incident beam is unpolarized. The in-plane and out-of-plane components of the electric field of the incident photons will be attenuated differently when they interact with the sample being measured. In polycrystalline samples this factor tends to overestimate peaks near the extremes of the measurement. At the high angle extremes of the range of the experiment the L-P factors for both powder and single crystal measurements converge, however other factors such as the Debye Temperature factor severely limit the intensity of the scattered beam at high angle, and

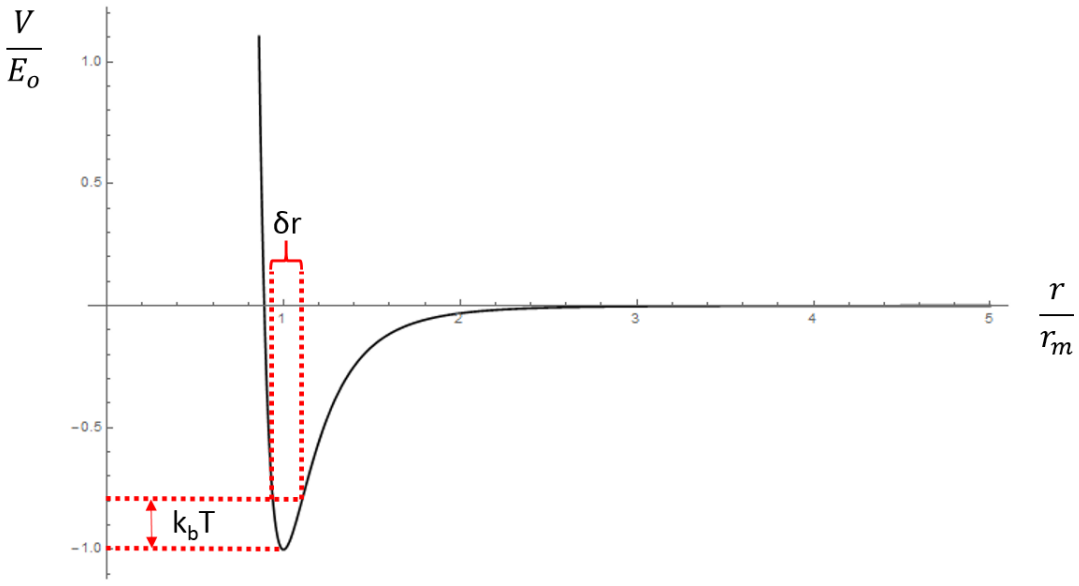

Figure 3.2. Lennard-Jones potential showing an atom's deviation from it's minimum potential due to temperature effects.

therefore an experimental comparison of the L-P factor at this range is unreliable.

In this way measuring the relative intensities of the peaks helps to differentiate single crystal patterns from those patterns that are simply textured (ie, polycrystalline but with preferred growth direction). In this work it is important that the measured samples are high quality single crystals, as transport and especially ARPES measurements are highly sensitive to disorder in the crystal structure.

To extract exact information from the diffraction pattern due to all these competing factors the use of Rietveld refinement is required. Rietveld refinement is a method to match the measured diffraction pattern against a theoretically modeled pattern using multiple parameters to simulate the exact diffraction pattern. Matching the theoretical model to the experimental model will provide very detailed information on the internal structure and crystalline nature of the sample in question. At this point the factors that contribute to a diffraction pattern are entirely solved and the theoretical model is highly reliable with practically no deviation from experimental results.

In general the integrated intensity of the diffraction pattern is given by Eqn 3.5 where I is the integrated intensity, F is the norm of the structure factor, m is the multiplicity of the hkl peak, L_p is the Lorentz-polarization factor and e^{-2M} is the Debye Temperature factor.

$$I_{hkl} = F_{hkl}^2 m_{hkl}(L_p)e^{-2M} \tag{3.5}$$

3.2.2 Experimental Factors

All X-ray Diffraction measurements in this work were done using a Rigaku Smart Lab device. X-rays were generated from a CuK_α source. X-rays are generated in the following way. Current is passed through a Tungsten filament such that electrons are emitted from the filament. A voltage is applied between the Tungsten filament and a Copper target so that the emitted electrons are accelerated toward the Copper target. The Copper target is then bombarded with electrons which produce two types of electromagnetic radiation. The first type of radiation is Bremsstrahlung radiation and is due to an electron passing by a Cu nucleus and being deflected. This deflection accelerates the electrons and therefore photons are emitted. This radiation is not characteristic of the material and is emitted in a broad spectrum. The second type of radiation is the characteristic emission for the material and is due to electrons in the Cu target jumping to lower energy states that were vacated during electron-electron collisions. K_α is the Siegbahn notation describing the orbital transition from the 2p to 1s state. Further considering spin-orbit interactions leads to a splitting of the K_α emission to $K_{\alpha 1}$ and $K_{\alpha 2}$ where $K_{\alpha 1}$ is the $2p_{\frac{3}{2}}$ to 1s transition and $K_{\alpha 2}$ is the $2p_{\frac{1}{2}}$ to 1s transition. The next allowed transition to the 1s state is from 3p to 1s. Due to the energy scale of the 3p orbital, the spin-orbit splitting is difficult to resolve in practice and so this characteristic peak is labeled simply as K_β. Due to the different emission energies of these transitions the generated photons will be produced at different wavelength, thereby

altering the Bragg angle for each hkl plane measured. This gives the effect of "echoes" in the diffraction data, where the same hkl peak will show up three times. This is not ideal, so some measures can be taken to reduce the intensity of these peaks, specifically K_β.

Luckily, there is an easy solution. In general, by introducing a foil of atomic number Z - 1 where Z is the atomic number of the element we are using to generate the characteristic X-rays, we can severely attenuate the K_β radiation. To understand why this works so well we have to consider the source of the energy scales responsible for the elements' emission lines, namely the Binding Energy of the electronic states. Given simple Coulomb interactions we can see that E_b is proportional to Z. The absorption spectrum for an element is governed by the Binding Energy of the electronic states. Incident photons with a sufficient energy to eject an electron will be absorbed while photons with insufficient energy will be unaffected. In the case of characteristic X-rays, the photon energies are governed by the difference in Binding Energies of the allowed state transitions. It turns out then that E_b of the Z - 1 element tends to fall between the K_α and K_β energies of the Z element.

$$K_\alpha^Z < E_{b,1s}^{Z-1} < K_\beta^Z \tag{3.6}$$

Due to this result, placing a foil of Ni in the path of X-rays generated by a Cu target will severely attenuate the K_β emissions while leaving the K_α X-rays relatively unscathed.

3.3 ANGLE-RESOLVED PHOTOEMISSION SPECTROSCOPY

A useful tool for evaluating the effect of TRS breaking on the surface states of a TI is Angle Resolved Photoemission Spectroscopy (ARPES). The basic principle behind ARPES is the photoelectric effect, for which Albert Einstein won the Nobel Prize in Physics in 1921. The Photoelectric effect is the measuring of a voltage across a conductor when light of certain frequencies shines on it. When the photons are energetic enough they can eject electrons from the surface of the metal. These electrons are known as

photo-electrons. The absence of the ejected electrons leaves the conductor positively charged, resulting in a voltage difference between the conductor and the ground. The energy and relative angle with which these photo-electrons are ejected with are what is measured in ARPES. In low-energy scans UV light (20-40eV per photon) is used to eject electrons with energies near the Fermi Energy. By measuring the angle with which the photo-electrons are ejected we can gain information as to what their momentum in the crystal was. Combining this with the energy of the ejected photo-electron we are able to accurately map the E(k) dispersion relationship of the electrons in the Brillouin zone. This gives us a real picture of the bandstructure of the electrons near the Fermi Energy, revealing the precise nature of the bulk bandgap and surface states.

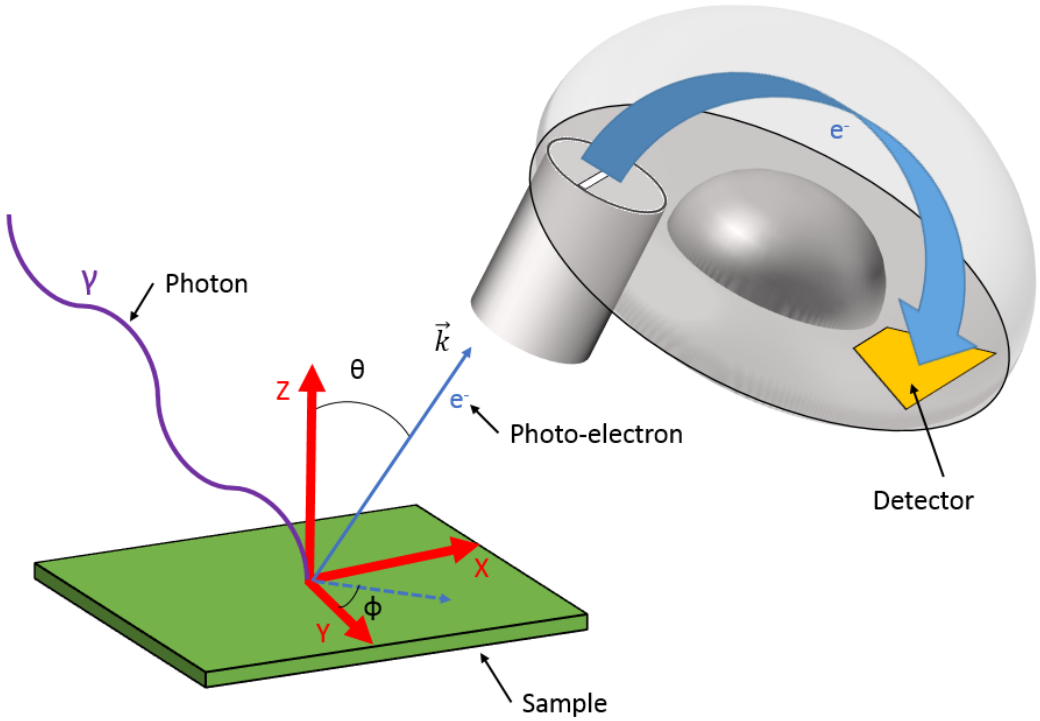

Figure 3.3. Schematic of ARPES device.

The energy (E) and deviated angle are measured at the detector. Given a specific photon energy $E_{ph} = h\nu$ and work function (ϕ_w) we can compute the binding energy of the photo-electron.

$$E_b = h\nu - E - \phi_w \tag{3.7}$$

And by relating the momentum of the photo-electron to its detected angle we can determine the wavenumber of the photo-electron.

$$\begin{aligned}
\vec{p} &= \hbar\vec{k} \\
\frac{p^2}{2m} &= E \\
p_z &= |p|cos(\theta) \\
p_y &= |p|sin(\theta)cos(\phi) \\
p_x &= |p|sin(\theta)sin(\phi) \\
k_z &= \hbar^{-1}\sqrt{2mE}cos(\theta) \\
k_y &= \hbar^{-1}\sqrt{2mE}sin(\theta)cos(\phi) \\
k_x &= \hbar^{-1}\sqrt{2mE}sin(\theta)sin(\phi)
\end{aligned} \tag{3.8}$$

Based on these equations we can see that the wavenumber-detector angle relationship scales with the photon energy. In a real measurement situation the sample may not be perfectly flat with respect to the perpendicular direction. This will manifest itself in slight deviations in the θ and ϕ angles. The problem then becomes how does one know where in the Brillouin is the data showing? Generally, in layered materials, the k_x and k_y directions are what are interesting, and Γ occurs at the value of $\theta = 0$. Then the location of Γ on the detector is independent of the photon energy. By taking measurements at multiple values of $h\nu$ one can then determine the location of Γ by observing the features which do not move as $h\nu$ is changed.

3.4 DENSITY FUNCTIONAL THEORY

To better understand the electronic nature of our system it is beneficial to model it computationally rather than continually making and measuring physical samples. To do this exactly one must solve the Schrödinger equation for a many-body system in a background potential.

$$\begin{gathered}(-\frac{1}{2}\nabla^2 + V_{ext}(\mathbf{r}) + V_{int}(\mathbf{r},\mathbf{r}^{'}))\mathbf{\Psi_i}(\mathbf{r}) = \epsilon_\mathbf{i}\mathbf{\Psi_i}(\mathbf{r}) \\ \downarrow \\ [T_e + V_{Ne} + V_{ee}]\Psi = E\Psi\end{gathered} \tag{3.9}$$

In particular we are considered with the V_{Ne} term, which is uniquely defined based on the system in question. This term defines the interaction of the electrons with the background potential. In our case the background potential is generated by the crystal structure of our material. Rather than computing the Schrödinger equation explicitly, we instead attempt to find a self-consistent charge density. [46, 47]

$$V_{Ne} = \int v(\mathbf{r})\psi^*(\mathbf{r})\psi(\mathbf{r})d\mathbf{r} \tag{3.10}$$

$$\rho(\mathbf{r}) = \sum_i \psi_i^*(\mathbf{r})\psi_i(\mathbf{r}) \tag{3.11}$$

Using equations (3.10) and (3.11) we can make an attempt to solve for the wavefunctions $\psi_i(\mathbf{r})$ in equation (3.9) by guessing at the form of $\rho(\mathbf{r})$ using our $v(\mathbf{r})$ generated by the structure of the crystal. Then, by using equation (3.11) to generate a new $\rho(\mathbf{r})$ based on the $\psi_i(\mathbf{r})$'s we can run the cycle again. Additionally this approach can be applied to the V_{ee} term in equation (3.9) by treating the electrons as probability densities given by $\rho(\mathbf{r})$. This exchange-correlation term then can be expressed as a functional of $\rho(\mathbf{r})$ as well.

$$V_{ee} = \frac{1}{2} \int \frac{\rho(\mathbf{r})\rho(\mathbf{r}')}{|\mathbf{r} - \mathbf{r}'|} d\mathbf{r} d\mathbf{r}' \tag{3.12}$$

Then, since Ψ is uniquely determined by ρ, then there exists a groundstate energy E_o such that ρ will returns itself on the next cycle, up to a constant. Then, as a self-consistent calculation, after several cycles the groundstate energy should converge to some finite value, and the difference in energies from one cycle to the next should approach zero. In practice zero is not a feasible convergence limit, so one must determine what convergence criteria is acceptable for the particular problem.

To solve these problems computationally the software used in this work was WIEN2K. WIEN2K uses an Augmented Plane Wave + Local Orbitals approach to generate solutions. [48] This code solves the Schödinger equation for both the core and valence electrons. Therefore it is necessary to determine criteria for what "core" and "valence" mean, mathematically. This is done by setting an energy difference between states such that, when the difference reaches the set point all states thereafter are regarded as valence electrons. And it is also necessary to use different bases for both situation. In the core electrons the potential and therefore wavefunctions are expanded in terms of spherical harmonics, and in the valence electrons the plane-wave basis is used.

$$\begin{aligned} V_{core} &= \sum_{lm} V_{lm}(r) Y_{lm}(\hat{\mathbf{r}}) \\ V_{val} &= \sum_{\mathbf{K}} V_{\mathbf{K}} e^{i\mathbf{K}\cdot\mathbf{r}} \end{aligned} \tag{3.13}$$

WIEN2K uses the procedures desribed by equations (3.10),(3.11) and (3.12) to produce solutions, however it must treat the core and valence densities separately, and then mix them at the end. In figure (3.4) we see that the WIEN2K code makes good use of the Hohenberg-Kohn and Kohn-Sham theorems. First, an initial ρ is calculated based on the input crystal structure of the system. Next that ρ is used to calculate inner and

outer potentials V_c and V_{xc}. Those potentials are then used to calculate the eigenstates and eigenvalues using Schödinger's equation. Those eigensates are then used to calculate the total probability densities ρ for the valence and core. These ρ's are then simply added together. Since these ρ's describe the densities in completely different regions of space, there is no overlap, and simply adding them gives an appropriate result for the total ρ. Next, these calculated ρ's are mixed with the ρ used to calculate the initial potentials, and a new ρ is generated. This process will continue until the energy difference in iterations reaches some threshold, as shown in equation (3.14). Once the calculations converge the eigenstates and eigenvalues can be used to generate the bandstructure of the material.

Putting the symmetries of the material into good use can significantly reduce the complexity of the Hamiltonians used to determine the eigenstates of the system. [14, 49]

$$|E[\rho_{new}] - E[\rho_{old}]| < E_{conv} \tag{3.14}$$

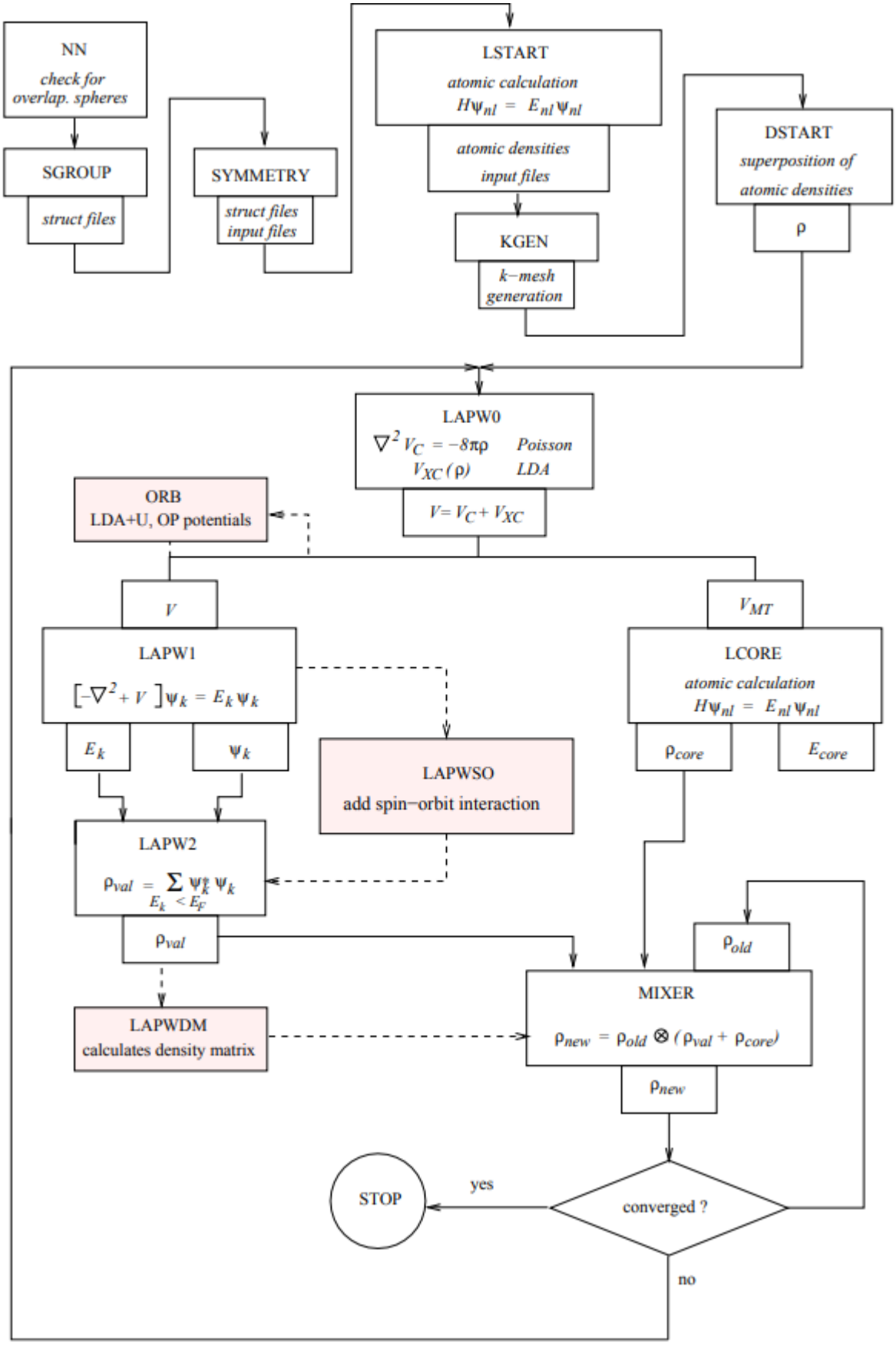

Figure 3.4. Flow chart of WIEN2K software.

CHAPTER 4

RESULTS

4.1 X-RAY DIFFRACTION

X-ray Diffraction was used to determine that the grown samples were the correct phase of Bi_2Se_3. By comparing the position of the peaks against the known pattern we can determine that the phase of the grown sample is Paraguanajuatite, which is the desired phase of Bi2Se3 in the R-3m spacegroup 166. Other species are possible which either share the same stoichiometry or spacegroup, however Paraguanajuatite is the only phase of its particular spacegroup and stoichiometry and is easily identified by its diffraction pattern. . The mechanical separation of flakes from the bulk ingot is characteristic of the layered nature of Bi_2Se_3 and suggests the single crystal nature of the sample by how large the separated flakes are.

Optical characterization is also strong, although insufficient, tool. As the bandgap for Bi_2Se_3 lies well within the Infrared range, the sample should reflect the visible spectrum, as can be seen in the Figure (4.1).

Another indication that the grown samples are high quality is the presence of high-angle peaks. Being able to identify high-angle peaks is important in measuring the changes in lattice parameter due to doping. In the figure below we see that the introduction of Gd to the sample results in a noticeable lattice expansion for the c parameter, contrary to others findings[37]

By comparing the Sm doped, Gd doped and simulated X-ray Diffraction patterns we can see that not only are the samples grown with a preferred orientation, but they are in fact single crystal. The simulated diffraction pattern is generated assuming a powder sample. Due to this we can see that the (003) peak in particular is highly favored in contrast to the relatively low intensity of that peak in the measured patterns. This is due to the difference in the L-P factor in powder and single crystal samples. We can also see that the presence of the dopants has not appreciably altered the structure of the parent

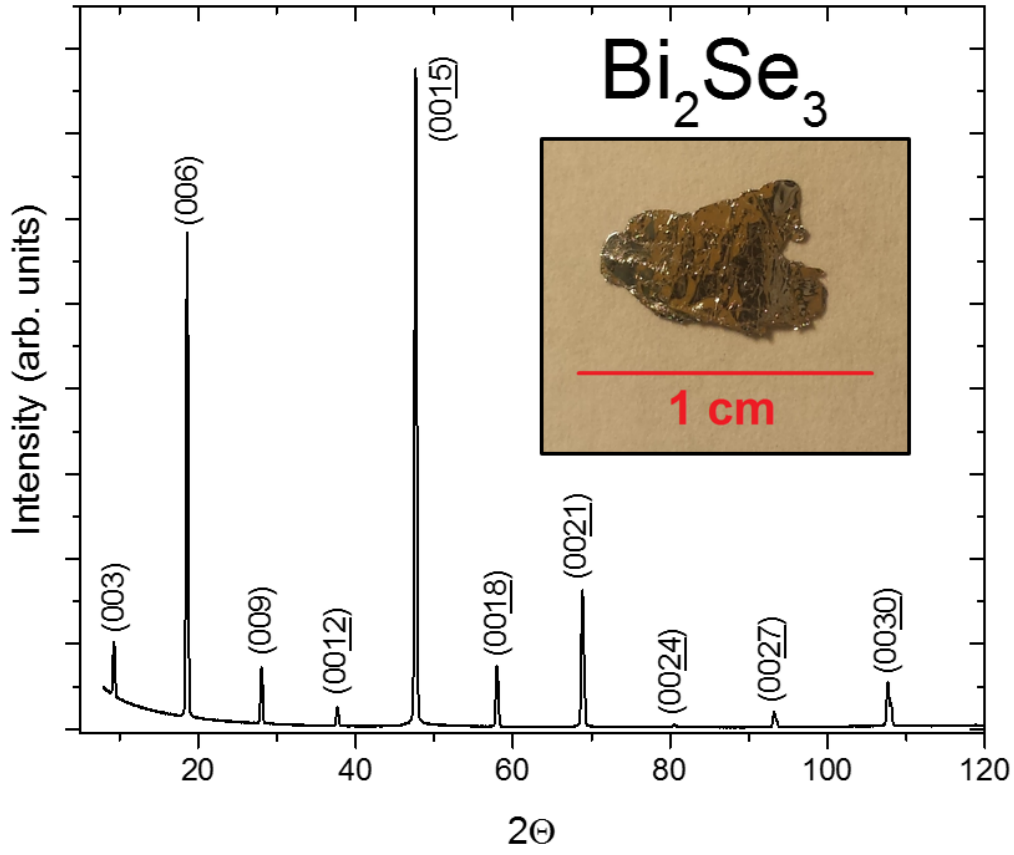

Figure 4.1. X-ray Diffraction data of Bi_2Se_3 showing (00L) texture. Inset: Optical image of Bi_2Se_3 flake.

compound.

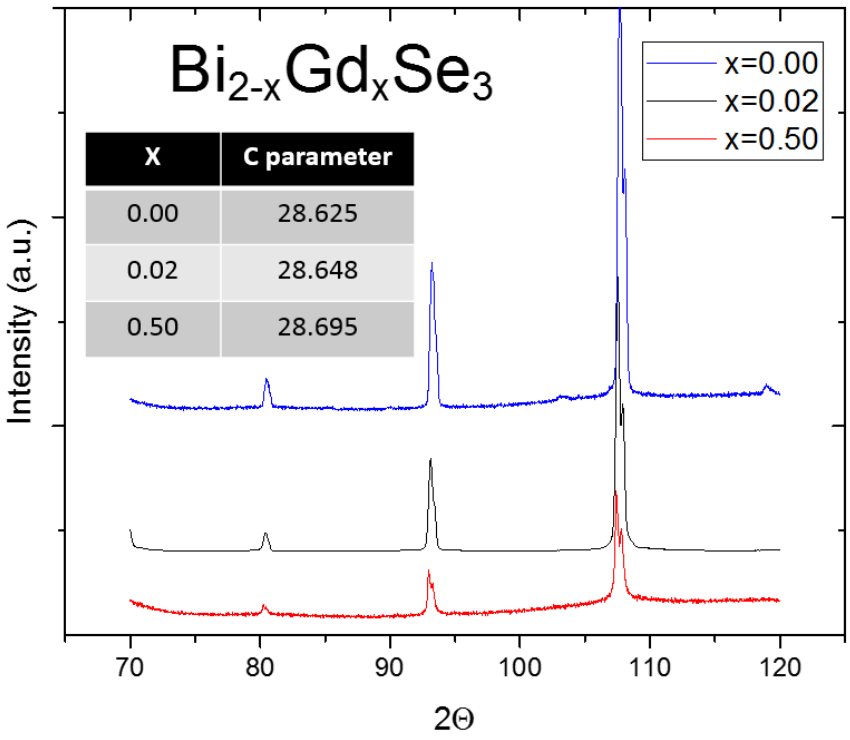

Figure 4.2. X-ray Diffraction data of $Bi_{2-x}Gd_xSe_3$ series. Inset: C Parameter measured at L=30 as a function of x.

4.2 ANGLE-RESOLVED PHOTOEMISSION SPECTROSCOPY

4.2.1 UV Sourced ARPES

ARPES measurements were performed at Missouri University at Columbia by Qiangsheng Lu in Dr. Guang Bian's laboratory. All measurements were taken at a temperature of 100K unless otherwise specified. The measurements also used a photon energy of 21.2 eV.

The expected result for the Gd doped Bi_2Se_3 ARPES data would show that the Dirac point remained preserved and the TSS would be gapless. In the case of the $Bi_{1.5}Gd_{0.5}Se_3$ data we can easily see that the Dirac point is present and the TSS are preserved. This is likely due to the high quality of the sample measured. In contrast the $Bi_{1.98}Gd_{0.02}Se_3$ data is much lower resolution, perhaps due to some imperfections in the

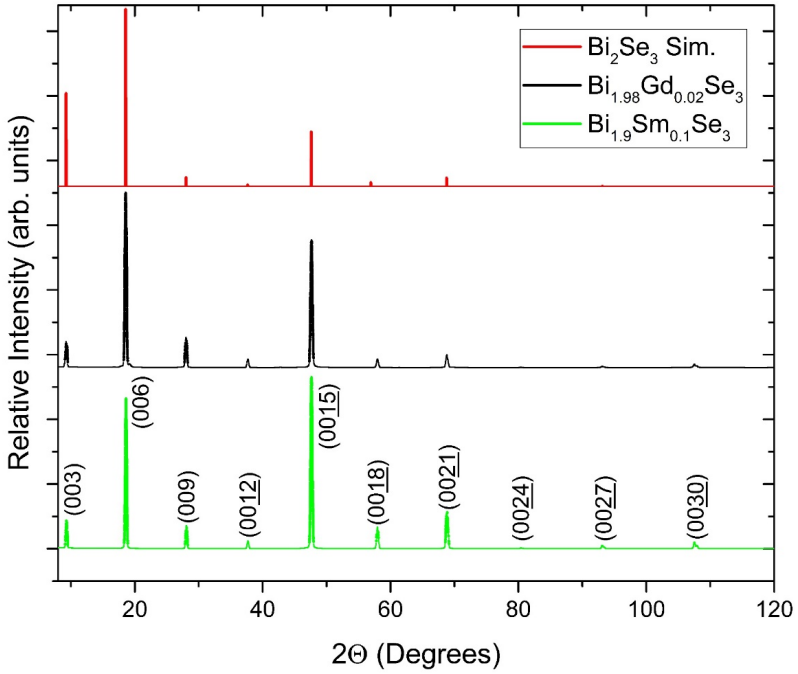

Figure 4.3. Comparison of Theoretical pattern with Gd and Sm doped Bi_2Se_3.

crystal. In both cases the VBM appears to be at -0.5 eV and the Dirac point at approximately -0.4 eV, giving a difference of 0.1 eV. Also worth noting is the location of the CBM just below -0.2 eV. The Spin-Orbit band inversion producing an indirect gap in the bandstructure is also present and the bandgap can be estimated at approximately 0.3 eV, which agrees with the literature. [50–54] It is concluded then that the magnetic ordering, if present in this system, has not broken the TRS of the parent compound as shown by the preservation of the TSS.

Next we consider the role magnetization plays in the Sm doped Bi_2Se_3 samples. In this case, in contrast to the Gd doped sample, the comparison was made between the same sample at two different temperatures rather than differing dopant concentrations. In this case the temperatures were chosen to be above and below the measured T_c of the material. The T_c of the sample $Bi_{1.9}Sm_{0.1}Se_3$ was measured to be approximately 250K.

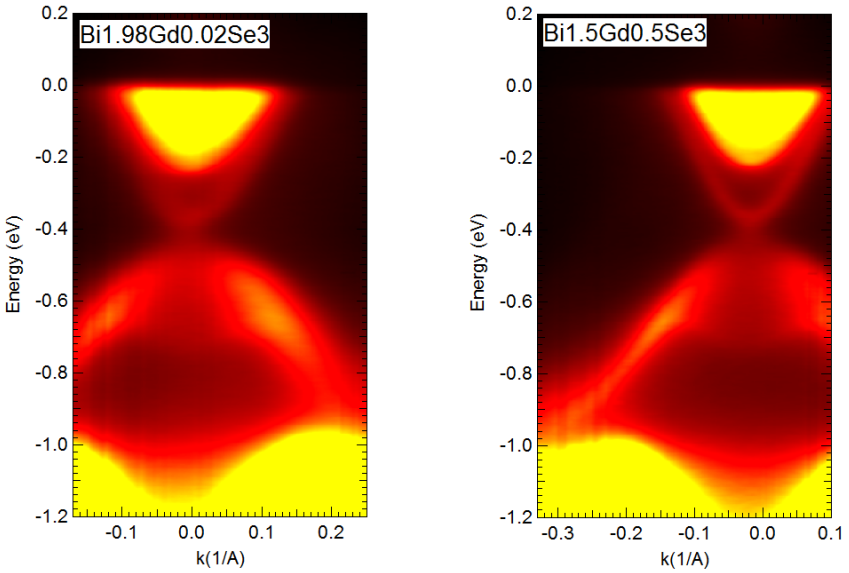

Figure 4.4. ARPES data of Bi_2Se_3 at different concentrations of Gd.

Therefore, when measuring the sample at a temperature of 300K there should be no ferromagnetic ordering to disrupt the TSS of the system. However what was found was that regardless of the temperature measured the TSS seems to be gapped. This gap is unlikely due to surface effects. [55, 56] Precisely what the energy value of this gap is cannot be determined from this data, however it appears to be on the order of 10 meV. The bulk band characteristics of the Sm doped sample also strongly agree with that of the Gd doped samples, suggesting no large scale effect on the parent compound as a whole. The presence of Sm seems to have only affected the nature of the surface states, which is an expected consequence of breaking TRS. It is therefore concluded that Sm doping has succeeded in breaking TRS in this system. However it appears that the presence of long-range FM ordering is not the only factor present in producing this effect. The TSS gap that exists at the 300K measurement may suggest that short-range magnetic ordering is also responsible for breaking TRS in this system. More magnetic measurements will be performed to determine the exact nature of the magnetic structure of this compound both above and below its T_c.

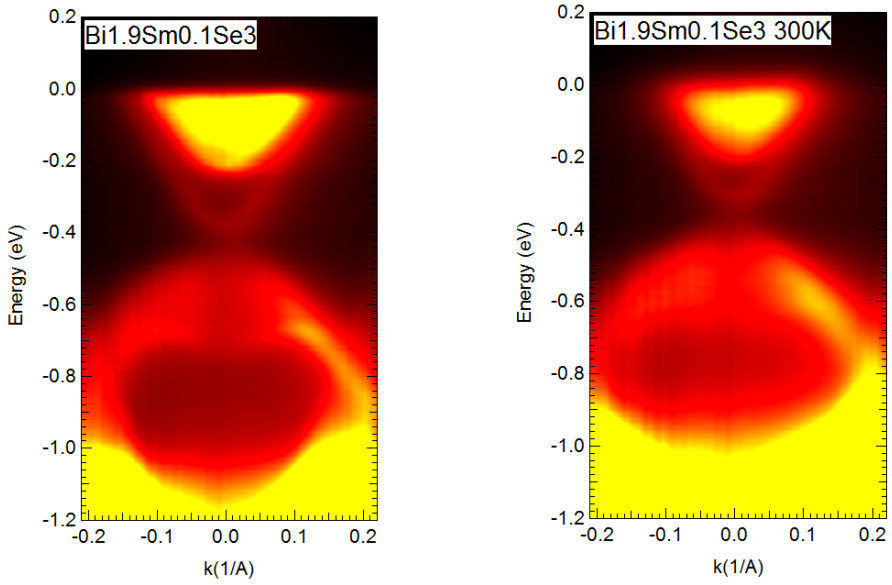

Figure 4.5. ARPES data of Sm doped Bi_2Se_3 above and below the T_c of the material.

4.2.2 Soft X-ray ARPES

ARPES work was also done at Argonne Nation Laboratory by the author of this work under the guidance of Jessica McChesney. There are many advantages to using Soft X-ray instead of UV light source. The main advantage is being able to probe larger energies in the bandstructure and as a result more of the Brillouin zone.

The downside to this is losing momentum resolution, as more of the Brillouin zone is represented in a fixed detector width. Another advantage is using the beamline to access a continuum of photon energies rather than fixed or very narrow spectra found in UV sources. Because of this, and the large photon energies available, the photon beam can be tuned to resonant binding energies of specific electronic states. For example, the binding energy of the Bismuth 4d electrons occur at approximately 440 eV, with some splitting because of spin-orbit coupling. This allows one to tune the energy to specific resonant energies in order to highlight the contributions of a specific electronic state to the mixed states found in the bandstructure. This experimental set-up also allows one to easily

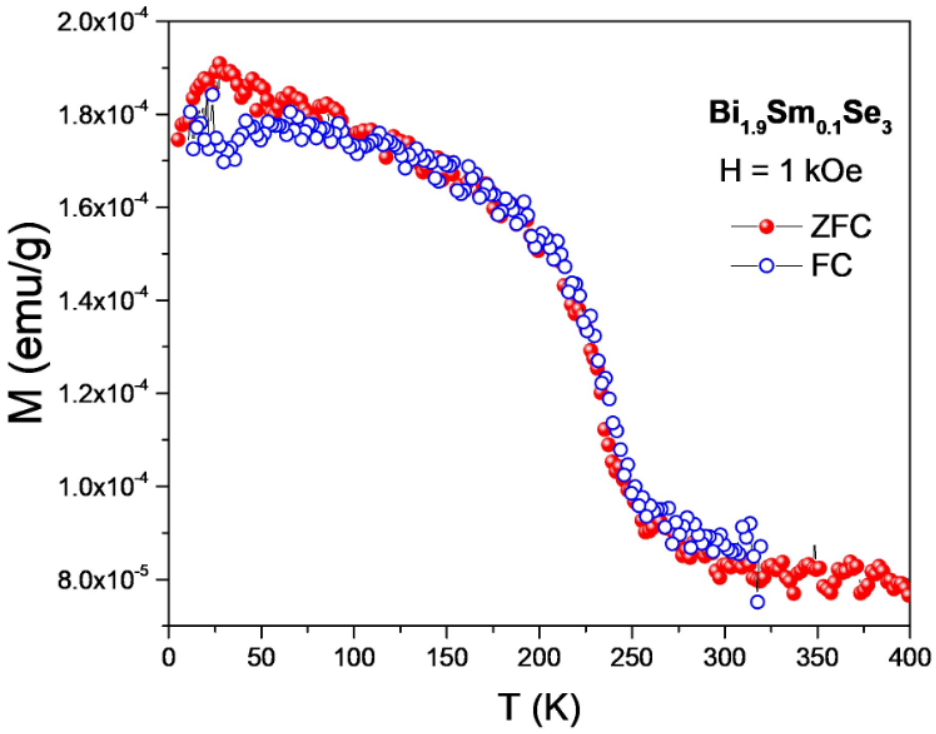

Figure 4.6. SQUID data showing the Curie Temperature of the Sm doped sample at nearly 250K.

determine the X-ray Photoemission Spectrum (XPS) of the sample by sweeping the beam energy through a large range and measuring the resonant energies corresponding to the electronic states present in the system.

For this work the samples measured were $Bi_{1.98}Gd_{0.02}Se_3$ and $Bi_{1.9}Sm_{0.1}Se_3$. All measurements were taken at 81K. Samples were cleaved in-situ at UHV pressures. The detector has an energy resolution of 0.0175 eV and an angular resolution of 0.03 degrees.

From the XPS data in Figure (4.7) we can determine the resonant energies which may be of interest in the ARPES scans. We can also determine the quality of the cleave in the measured sample. By observing the sharpness of the Bi 4f peaks we can see that it is indeed terminated in a Se layer[57–59], which is what we would expect for van der Waals materials. Multiple photon energies were used in the ARPES scans. To isolate the Bi $4d_{5/2}$ the photon energy was tuned to 440 eV. Other energies used were 400, 500, and

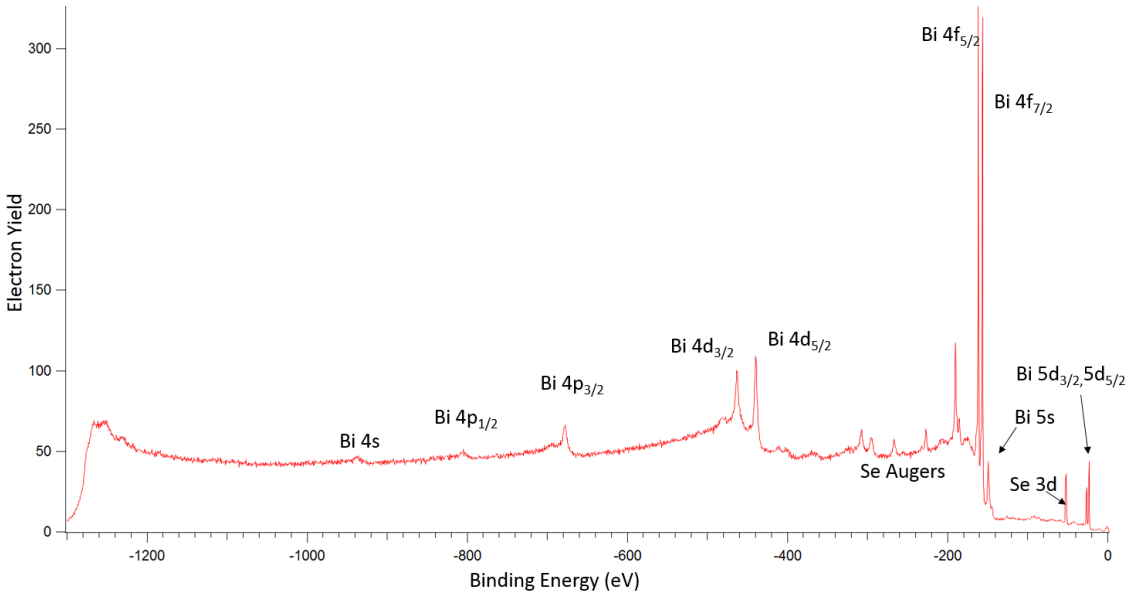

Figure 4.7. XPS measurement of Gd doped Bi_2Se_3.

550 eV.

Looking at Figure (4.8) we can see the evolution of the bandstructure shifting as the photon energy changes. This effect is described in Eqn. (3.8) where the photon energy E dictates the scale of the wavenumber to the corresponding detector angle. At these energies it appears that multiple Γ points are measured. By noticing a shift in the location of these Γ points as the photon energy changes we can determine that these are not located in the first Brillouin zone, where Γ is described by $\vec{k} = 0$.

Although our view of the conduction band is limited by the work function, we can still see a large part of the valence band. A small contribution from the conduction band surface states can still be seen indicating that the Gd doped samples appear to be gapless. Also, worth noting is the Bi $4d_{5/2}$ states highlighted in the 440 eV image appear to not be highly represented in the valence band surface states, preferring to rest in the lower bulk valence band states near Γ. We will return to this feature later when discussing DFT calculations and where we expect to see contributions from each electronic state.

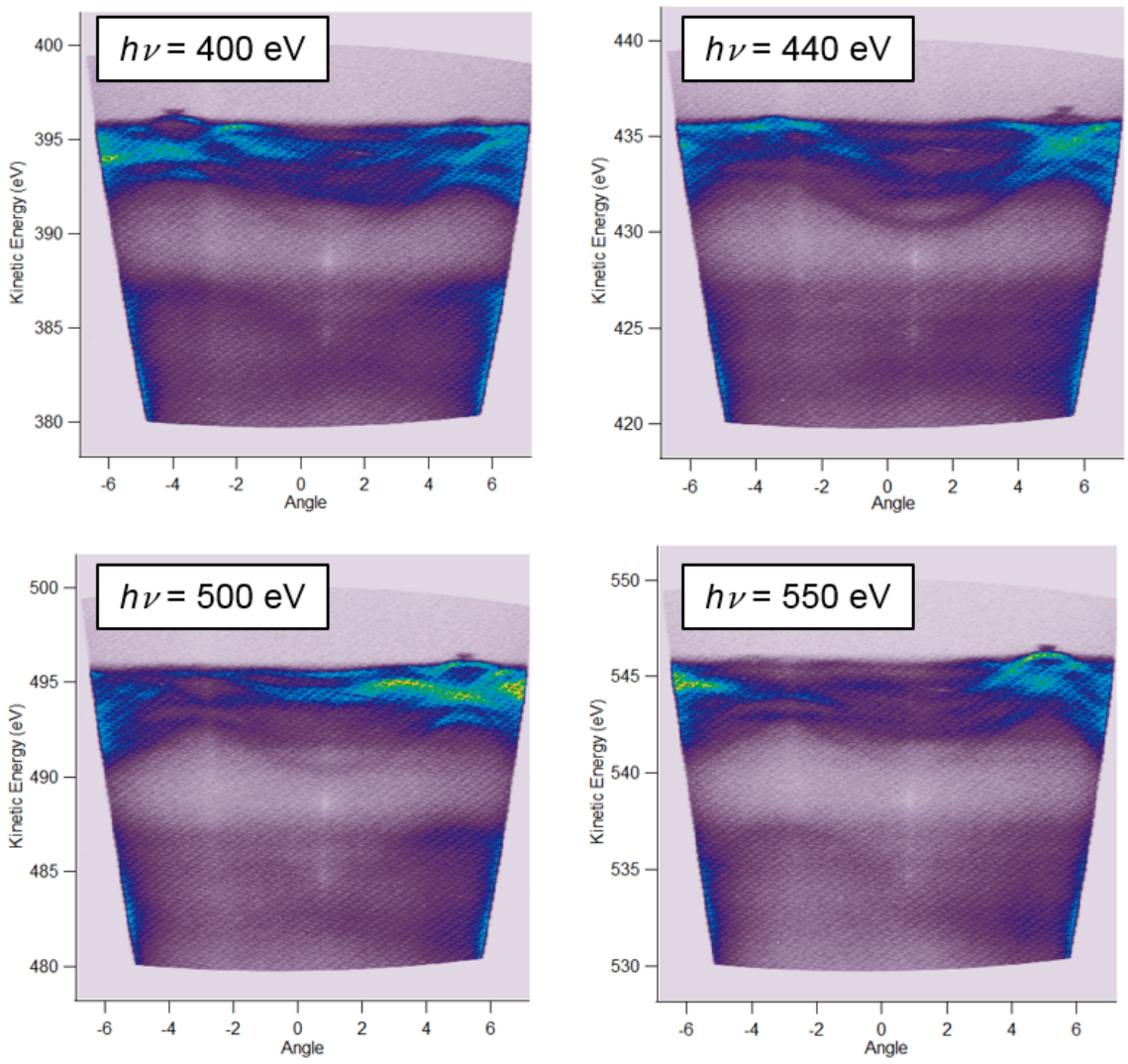

Figure 4.8. Resonant ARPES of Gd doped Bi_2Se_3.

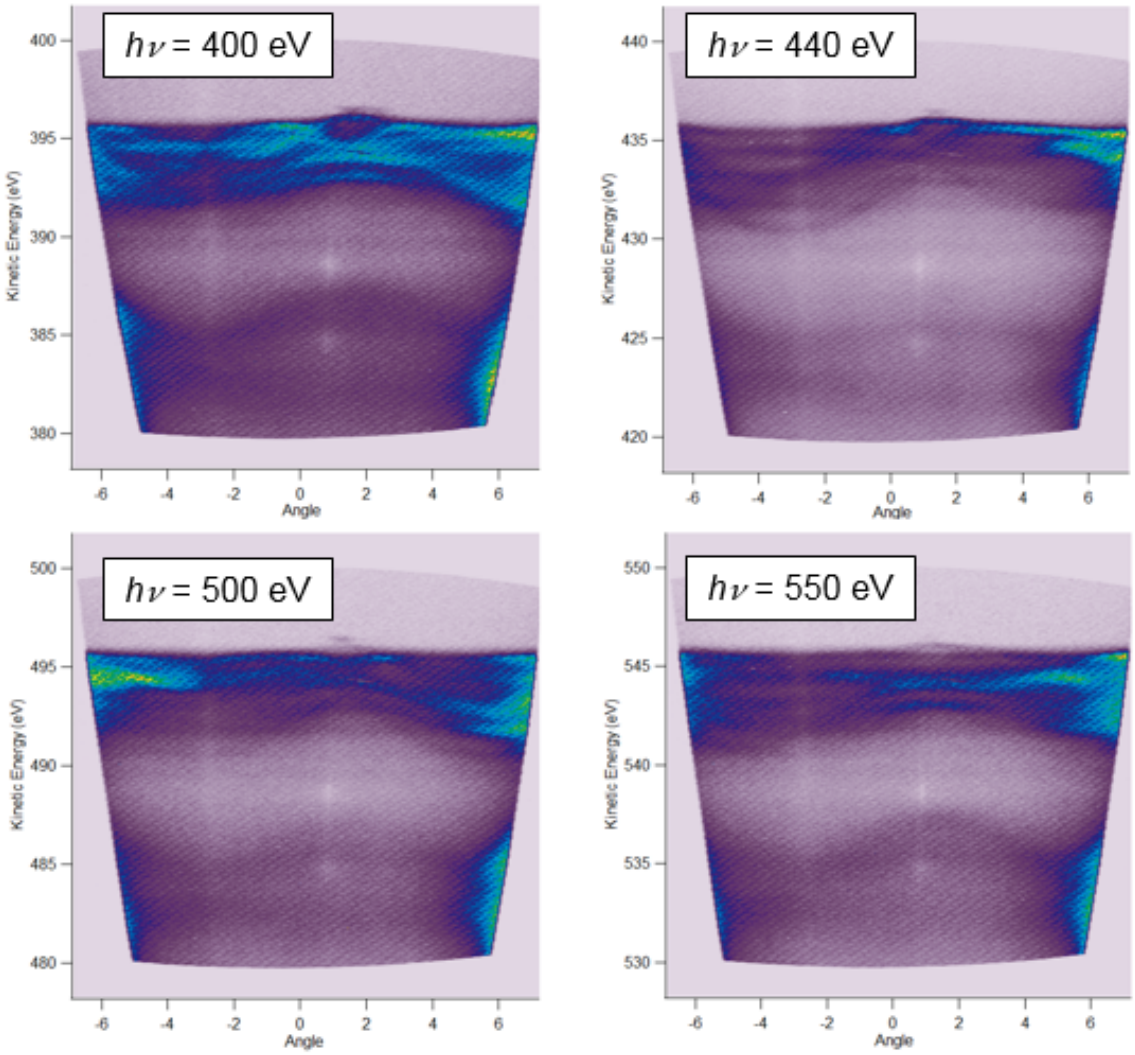

Figure 4.9. Resonant ARPES of Sm doped Bi_2Se_3.

In the Sm doped data shown in Figure (4.9) we see some differences to the Figure (4.8). The two major differences are first, the overall intensity of the signal. The Sm doped sample is much noisier suggesting that the crystal quality is overall poorer. Second, is the location of the Γ point. In the Sm sample Γ doesn't seem to move as the photon energy changes, suggesting that were are looking at Γ in the first Brillouin zone. Also worth noting is the appearance of what seems to be a gap in the surface states. While this is inconclusive by itself due to various experimental factors at play, taken with the UV ARPES and MvT data we can say with good certainty that there is a gap in the TSS due to the presence of Sm in the sample.

4.2.3 DFT Bandstructure

All DFT calculations were performed using the WIEN2K software utilizing the LAPW method. For bulk characterization the structure used was spacegroup 166, R-3m in rhombohedral axes. The generated k-mesh is 10x10x10, RMT is set to 2.5 for both Se and Bi, and RKmax is 6. Calculations were done using the GGA [60] potential with an energy convergence of 0.0001 Ry.

Figure (4.10) shows the structure of Bi_2Se_3 in both Rhombohedral and Hexagonal axes. The Rhombohedral representation is the primitive unit cell, while the Hexagonal unit cell is the more conventional representation. The Hexagonal structure in Figure (4.10) has been extended in the xy plane to accent its layered nature. The mirror symmetry in the z-direction is clearly shown in the Hexagonal representation, while the three-fold rotation symmetry in the xy plane is easily seen in the Rhombohedral axes. These symmetries are valuable for DFT calculations as they reduce the computational requirements for the system.

DFT calculations were done on this structure with and without SOC to determine the role SOC plays in the shape of the bandstructure. For SOC calculations all atoms were considered to have SOC effects. However, due to its large local potential Bi radial

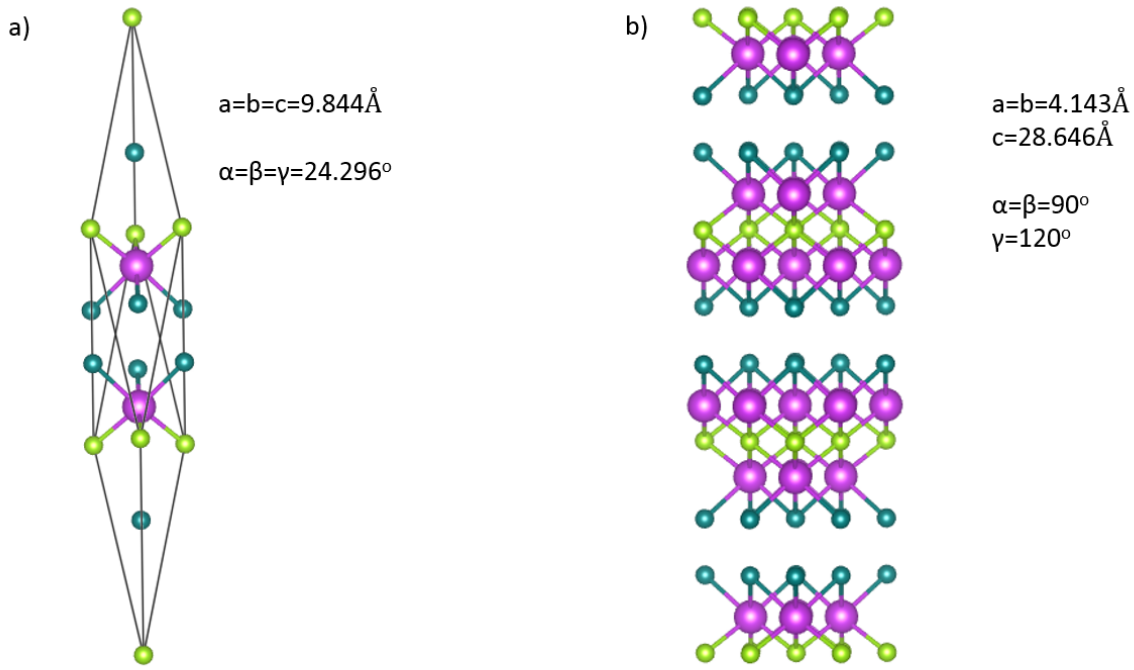

Figure 4.10. Visual representation of Bi_2Se_3 in a) R and b) H axes.

states may become split between the core and valence. For this reason an $p_{1/2}$ RLO state was added to Bi to improve its basis.

As can be seen in Figure (4.11) the SOC changes the material from a direct gapped system to an indirect gap of about 0.35 eV. Degeneracies present in the non-SOC calculation are lifted in the SOC case. Additionally, the CBM and VBM at Γ have swapped places due to the band inversion introduced with the SOC effect. In particular the Bi p_z and Se p_z orbitals have inverted.

Figure (4.12) shows the role SOC plays in the inversion of the p_z orbitals. The circles represent the magnitude of the projection of the eigenvector onto the p_z basis. A larger circle then means that the p_z state is highly represented in that particular band. For the non-SOC calculations we can see that the Bi and Se p_z bands are segregated into the conduction and valence bands, respectively. Very little mixing occurs when SOC is not

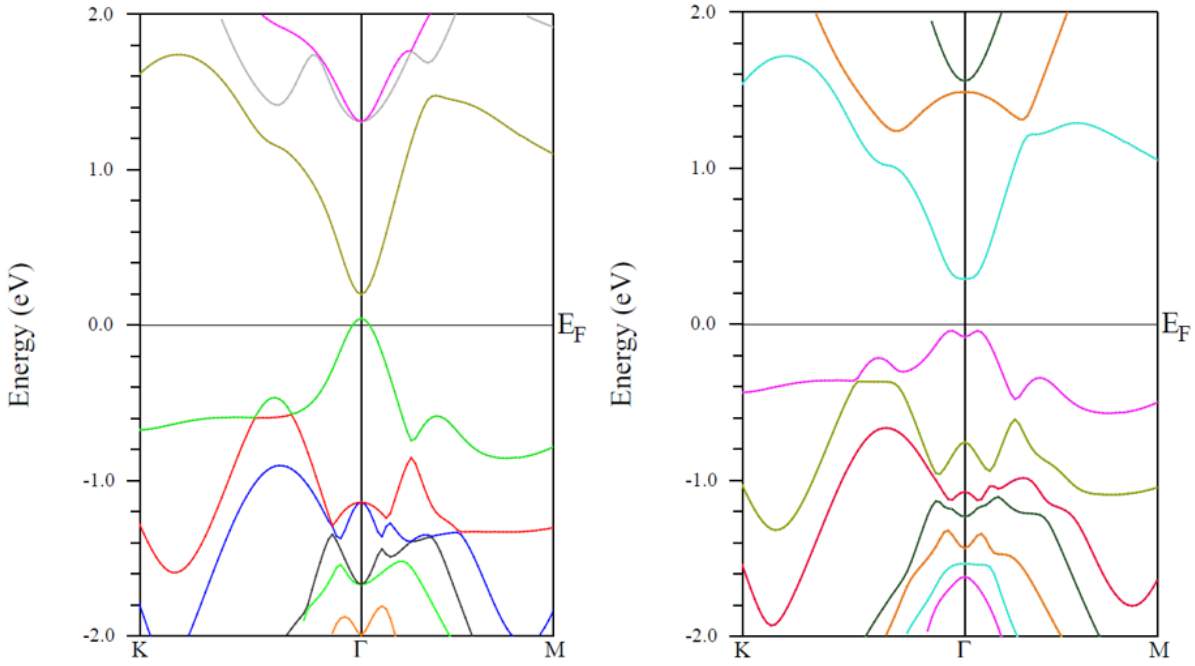

Figure 4.11. Bandstructure of Bi_2Se_3 without and with SOC, respectively.

considered. With SOC turned on we can see that the bands get very mixed near Γ. The dip near Γ in the valence band in the SOC case is highly represented by Bi p_z which can be explained by the CBM in the non-SOC case moving down due to the effects of SOC. Also, the conduction band near Γ in SOC case is heavily Se p_z favored, whereas in the non-SOC there was practically no representation of that basis. Due to this inversion around the Γ point there should be a non-trivial Berry's Phase which will manifest itself by the presence of a Dirac Cone at Γ when the surface interfaces with a trivial topological material, such as a vacuum.

Using DFT analysis we can also determine what direction were are measuring along in our ARPES data. In Figure (4.8) we looked at Gd doped Bi_2Se_3 ARPES. It is apparent that there are two Γ points in our measurement range, and due to the size of our measuremet range that these two Γ points are in neighboring Brillouin zones. Therefore it should be evident that this measurement is taken very near to a high

symmetry direction, and the midpoint between these two Γ points is also a high symmetry point, namely K or M. By comparing the DFT Bandstructure to the ARPES data we can determine which direction this measurement is actually taken along.

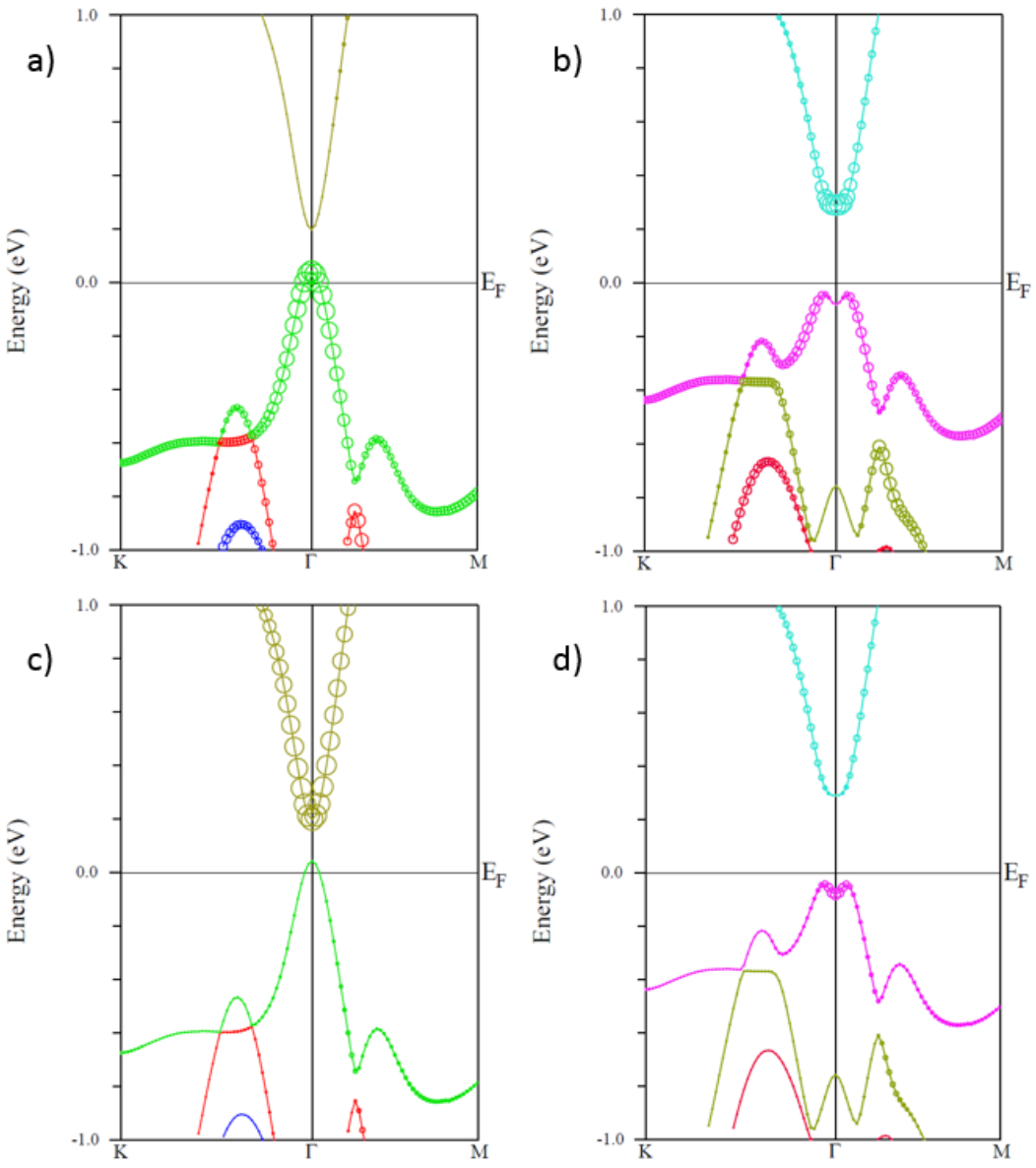

Figure 4.12. Inversion of the p_z orbitals with SOC. a) Se p_z without SOC, b) Se p_z with SOC, c) Bi p_z without SOC, d) Bi p_z with SOC.

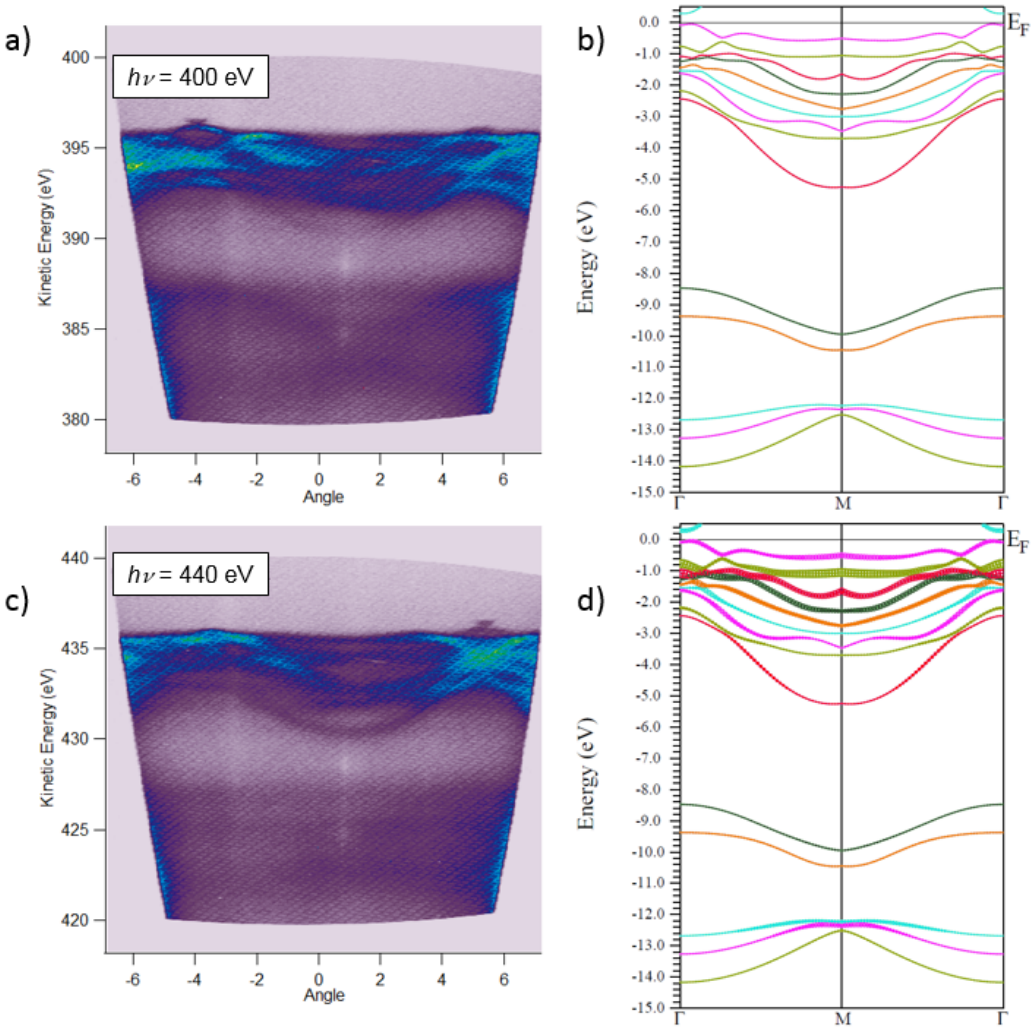

Figure 4.13. Comparison of DFT and ARPES Bandstructure. a) Gd doped Bi_2Se_3 ARPES at 400 eV. b) DFT of Bi_2Se_3. c) Gd doped Bi_2Se_3 ARPES at Bi $4d_{5/2}$ resonance 440 eV. d) DFT of Bi_2Se_3 highlighting Bi d orbitals.

CHAPTER 5

CONCLUSION

5.1 RESTATEMENT OF HYPOTHESIS

This work has focused on the synthesis and characterization of Gd and Sm doped Bi_2Se_3. It is then expected that with enough Gd doping the system will form an AFM phase with a $T_N < 10$K. The result of this will be that TRS will be broken locally at the impurity sites, but the metallic TSS should be conserved throughout the material. Also, due to the unique topological spin-texture present in the system, this AFM phase may show novel long-range order. In the Sm doped sample it is expected that a FM phase will form with a T_C near 50K, breaking TRS throughout the system and thereby inducing a gap in the TSS. A consequence of this would be the formation of a QAHE state in the system, which will require more thorough investigation.

5.2 CONCLUSION

5.2.1 Validity of Results

The quality of samples in this work is the major source of error in the results. Due to this much care in characterization of the samples was necessary to ensure the quality of the work. From the X-ray Diffraction data we can be sure that the samples grown were in fact single crystal without any spurious phases in competition with the main Paraguanajuatite phase. Also, where applicable in the ARPES measurements, the quality of the crystal is self-evident by the fact that clear bands are shown. If the crystal were poly-crystalline then band dispersion along specific momentas would not be shown, and the data would shown merely the density of states as a function of energy.

5.2.2 AFM Character of Gd doped Bi_2Se_3

The lack of a gap in the ARPES data is an inconclusive result for the presence of an AFM ordering in Gd doped samples. More magnetic measurements and DFT analysis will be required to determine the expected behaviour of the TSS's due to AFM ordering in the sample.

5.2.3 FM Character of Sm doped Bi_2Se_3

The appearance of a gap in the ARPES data is an expected result for FM ordering in Sm doped samples. The smearing of the bands in both the UV and Soft X-ray scans is likely a result of some minor disorder in the samples. Due to this the exact value of the TSS gap is difficult to determine. However it is also clear due to the more parabolic dispersion of the bands, particularly above the Dirac point, the magnetic ordering has induced some mass in the system. The nature of the TSS gap above the Curie temperature however is somewhat puzzling and will require more thorough investigation.

5.2.4 Future Work

With the continuation of this work the next appropriate step will be to synthesize materials which will be good candidates for measuring the QAHE. To this end the main goals will be to 1) Control the carrier concentration with doping, likely with Sb replacing Bi along with providing a Se rich environment to reduce vacancies, 2) More rigorously probe the magnetic behavior of Sm doped samples through SQUID, and 3) Determine more accurately describe the AFM phase of Gd doped samples with Neutron Scattering.

REFERENCES

[1] E. H. Hall. On a new action of the magnet on electric currents. *American Journal of Mathematics*, 2(3):287–292, 1879. ISSN 00029327, 10806377. URL http://www.jstor.org/stable/2369245.

[2] F. D. M. Haldane. Model for a quantum hall effect without landau levels: Condensed-matter realization of the "parity anomaly". *Phys. Rev. Lett.*, 61: 2015–2018, Oct 1988. doi: 10.1103/PhysRevLett.61.2015. URL https://link.aps.org/doi/10.1103/PhysRevLett.61.2015.

[3] Peng Cheng, Canli Song, Tong Zhang, Yanyi Zhang, Yilin Wang, Jin-Feng Jia, Jing Wang, Yayu Wang, Bang-Fen Zhu, Xi Chen, Xucun Ma, Ke He, Lili Wang, Xi Dai, Zhong Fang, Xincheng Xie, Xiao-Liang Qi, Chao-Xing Liu, Shou-Cheng Zhang, and Qi-Kun Xue. Landau quantization of topological surface states in bi_2se_3. *Phys. Rev. Lett.*, 105:076801, Aug 2010. doi: 10.1103/PhysRevLett.105.076801. URL https://link.aps.org/doi/10.1103/PhysRevLett.105.076801.

[4] V. P. Gusynin and S. G. Sharapov. Unconventional integer quantum hall effect in graphene. *Phys. Rev. Lett.*, 95:146801, Sep 2005. doi: 10.1103/PhysRevLett.95.146801. URL https://link.aps.org/doi/10.1103/PhysRevLett.95.146801.

[5] Tsuneya Ando and Yasutada Uemura. Theory of quantum transport in a two-dimensional electron system under magnetic fields. i. characteristics of level broadening and transport under strong fields. *Journal of the Physical Society of Japan*, 36(4):959–967, 1974. doi: 10.1143/JPSJ.36.959. URL https://doi.org/10.1143/JPSJ.36.959.

[6] K. v. Klitzing, G. Dorda, and M. Pepper. New method for high-accuracy determination of the fine-structure constant based on quantized hall resistance.

Phys. Rev. Lett., 45:494–497, Aug 1980. doi: 10.1103/PhysRevLett.45.494. URL https://link.aps.org/doi/10.1103/PhysRevLett.45.494.

[7] R. B. Laughlin. Anomalous quantum hall effect: An incompressible quantum fluid with fractionally charged excitations. *Phys. Rev. Lett.*, 50:1395–1398, May 1983. doi: 10.1103/PhysRevLett.50.1395. URL https://link.aps.org/doi/10.1103/PhysRevLett.50.1395.

[8] Kevin F. Garrity and David Vanderbilt. Chern insulators from heavy atoms on magnetic substrates. *Phys. Rev. Lett.*, 110:116802, Mar 2013. doi: 10.1103/PhysRevLett.110.116802. URL https://link.aps.org/doi/10.1103/PhysRevLett.110.116802.

[9] D. Hsieh, D. Qian, L. Wray, Y. Xia, Y. S. Hor, R. J. Cava, and M. Z. Hasan. A topological dirac insulator in a quantum spin hall phase. *Nature*, 452:970 EP –, Apr 2008. URL http://dx.doi.org/10.1038/nature06843.

[10] A. J. Heeger, S. Kivelson, J. R. Schrieffer, and W. P. Su. Solitons in conducting polymers. *Rev. Mod. Phys.*, 60:781–850, Jul 1988. doi: 10.1103/RevModPhys.60.781. URL https://link.aps.org/doi/10.1103/RevModPhys.60.781.

[11] M. V. Berry, F. R. S. Quantal phase factors accompanying adiabatic changes. *Proceedings of the Royal Society of London A: Mathematical, Physical and Engineering Sciences*, 392(1802):45–57, 1984. ISSN 0080-4630. doi: 10.1098/rspa.1984.0023. URL http://rspa.royalsocietypublishing.org/content/392/1802/45.

[12] B. Andrei Bernevig, Taylor L. Hughes, and Shou-Cheng Zhang. Quantum Spin Hall Effect and Topological Phase Transition in HgTe Quantum Wells. *Science*, 314 (5806):1757–1761, 2006. ISSN 0036-8075. doi: 10.1126/science.1133734. URL http://science.sciencemag.org/content/314/5806/1757.

[13] C. L. Kane and E. J. Mele. Z_2 topological order and the quantum spin hall effect. *Phys. Rev. Lett.*, 95:146802, Sep 2005. doi: 10.1103/PhysRevLett.95.146802. URL https://link.aps.org/doi/10.1103/PhysRevLett.95.146802.

[14] Yoichi Ando. Topological insulator materials. *Journal of the Physical Society of Japan*, 82(10):102001, 2013. doi: 10.7566/JPSJ.82.102001. URL https://doi.org/10.7566/JPSJ.82.102001.

[15] Rui Yu, Wei Zhang, Hai-Jun Zhang, Shou-Cheng Zhang, Xi Dai, and Zhong Fang. Quantized anomalous hall effect in magnetic topological insulators. *Science*, 329 (5987):61–64, 2010. ISSN 0036-8075. doi: 10.1126/science.1187485. URL http://science.sciencemag.org/content/329/5987/61.

[16] Masaru Onoda and Naoto Nagaosa. Quantized anomalous hall effect in two-dimensional ferromagnets: Quantum hall effect in metals. *Phys. Rev. Lett.*, 90: 206601, May 2003. doi: 10.1103/PhysRevLett.90.206601. URL https://link.aps.org/doi/10.1103/PhysRevLett.90.206601.

[17] Chao-Xing Liu, Xiao-Liang Qi, Xi Dai, Zhong Fang, and Shou-Cheng Zhang. Quantum anomalous hall effect in $\mathrm{hg}_{1-y}\mathrm{mn}_y\mathrm{Te}$ quantum wells. *Phys. Rev. Lett.*, 101: 146802, Oct 2008. doi: 10.1103/PhysRevLett.101.146802. URL https://link.aps.org/doi/10.1103/PhysRevLett.101.146802.

[18] Zhenhua Qiao, Wei Ren, Hua Chen, L. Bellaiche, Zhenyu Zhang, A. H. MacDonald, and Qian Niu. Quantum anomalous hall effect in graphene proximity coupled to an antiferromagnetic insulator. *Phys. Rev. Lett.*, 112:116404, Mar 2014. doi: 10.1103/PhysRevLett.112.116404. URL https://link.aps.org/doi/10.1103/PhysRevLett.112.116404.

[19] Hongbin Zhang, Cesar Lazo, Stefan Blügel, Stefan Heinze, and Yuriy Mokrousov. Electrically tunable quantum anomalous hall effect in graphene decorated by $5d$

transition-metal adatoms. *Phys. Rev. Lett.*, 108:056802, Feb 2012. doi: 10.1103/PhysRevLett.108.056802. URL https://link.aps.org/doi/10.1103/PhysRevLett.108.056802.

[20] Kentaro Nomura and Naoto Nagaosa. Surface-quantized anomalous hall current and the magnetoelectric effect in magnetically disordered topological insulators. *Phys. Rev. Lett.*, 106:166802, Apr 2011. doi: 10.1103/PhysRevLett.106.166802. URL https://link.aps.org/doi/10.1103/PhysRevLett.106.166802.

[21] Chi Tang, Bin Cheng, Mohammed Aldosary, Zhiyong Wang, Zilong Jiang, K. Watanabe, T. Taniguchi, Marc Bockrath, and Jing Shi. Approaching quantum anomalous hall effect in proximity-coupled yig/graphene/h-bn sandwich structure. *APL Materials*, 6(2):026401, 2018. doi: 10.1063/1.5001318. URL https://doi.org/10.1063/1.5001318.

[22] Z.-H. Zhu, G. Levy, B. Ludbrook, C. N. Veenstra, J. A. Rosen, R. Comin, D. Wong, P. Dosanjh, A. Ubaldini, P. Syers, N. P. Butch, J. Paglione, I. S. Elfimov, and A. Damascelli. Rashba spin-splitting control at the surface of the topological insulator bi_2se_3. *Phys. Rev. Lett.*, 107:186405, Oct 2011. doi: 10.1103/PhysRevLett.107.186405. URL https://link.aps.org/doi/10.1103/PhysRevLett.107.186405.

[23] L. Andrew Wray, Su-Yang Xu, Yuqi Xia, David Hsieh, Alexei V. Fedorov, Yew San Hor, Robert J. Cava, Arun Bansil, Hsin Lin, and M. Zahid Hasan. A topological insulator surface under strong coulomb, magnetic and disorder perturbations. *Nature Physics*, 7:32 EP –, Dec 2010. URL http://dx.doi.org/10.1038/nphys1838.

[24] L. Andrew Wray, Su-Yang Xu, Yuqi Xia, Yew San Hor, Dong Qian, Alexei V. Fedorov, Hsin Lin, Arun Bansil, Robert J. Cava, and M. Zahid Hasan. Observation

of topological order in a superconducting doped topological insulator. *Nature Physics*, 6:855 EP –, Sep 2010. URL http://dx.doi.org/10.1038/nphys1762.

[25] Liang Fu and Erez Berg. Odd-parity topological superconductors: Theory and application to $cu_x bi_2 se_3$. *Phys. Rev. Lett.*, 105:097001, Aug 2010. doi: 10.1103/PhysRevLett.105.097001. URL https://link.aps.org/doi/10.1103/PhysRevLett.105.097001.

[26] Liang Fu and C. L. Kane. Superconducting proximity effect and majorana fermions at the surface of a topological insulator. *Phys. Rev. Lett.*, 100:096407, Mar 2008. doi: 10.1103/PhysRevLett.100.096407. URL https://link.aps.org/doi/10.1103/PhysRevLett.100.096407.

[27] Liang Fu and C. L. Kane. Probing neutral majorana fermion edge modes with charge transport. *Phys. Rev. Lett.*, 102:216403, May 2009. doi: 10.1103/PhysRevLett.102.216403. URL https://link.aps.org/doi/10.1103/PhysRevLett.102.216403.

[28] K. T. Law, Patrick A. Lee, and T. K. Ng. Majorana fermion induced resonant andreev reflection. *Phys. Rev. Lett.*, 103:237001, Dec 2009. doi: 10.1103/PhysRevLett.103.237001. URL https://link.aps.org/doi/10.1103/PhysRevLett.103.237001.

[29] Xiao-Liang Qi, Rundong Li, Jiadong Zang, and Shou-Cheng Zhang. Inducing a magnetic monopole with topological surface states. *Science*, 323(5918):1184–1187, 2009. ISSN 0036-8075. doi: 10.1126/science.1167747. URL http://science.sciencemag.org/content/323/5918/1184.

[30] Dung-Hai Lee. Surface states of topological insulators: The dirac fermion in curved two-dimensional spaces. *Phys. Rev. Lett.*, 103:196804, Nov 2009. doi:

10.1103/PhysRevLett.103.196804. URL https://link.aps.org/doi/10.1103/PhysRevLett.103.196804.

[31] Y. L. Chen, J. G. Analytis, J.-H. Chu, Z. K. Liu, S.-K. Mo, X. L. Qi, H. J. Zhang, D. H. Lu, X. Dai, Z. Fang, S. C. Zhang, I. R. Fisher, Z. Hussain, and Z.-X. Shen. Experimental realization of a three-dimensional topological insulator, bi2te3. *Science*, 325(5937):178–181, 2009. ISSN 0036-8075. doi: 10.1126/science.1173034. URL http://science.sciencemag.org/content/325/5937/178.

[32] Y. Xia, D. Qian, D. Hsieh, L. Wray, A. Pal, H. Lin, A. Bansil, D. Grauer, Y. S. Hor, R. J. Cava, and M. Z. Hasan. Observation of a large-gap topological-insulator class with a single dirac cone on the surface. *Nature Physics*, 5:398 EP –, May 2009. URL http://dx.doi.org/10.1038/nphys1274.

[33] Mao Ye, Wei Li, Siyuan Zhu, Yukiharu Takeda, Yuji Saitoh, Jiajia Wang, Hong Pan, Munisa Nurmamat, Kazuki Sumida, Fuhao Ji, Zhen Liu, Haifeng Yang, Zhengtai Liu, Dawei Shen, Akio Kimura, Shan Qiao, and Xiaoming Xie. Carrier-mediated ferromagnetism in the magnetic topological insulator cr-doped (sb,bi)2te3. *Nature Communications*, 6:8913 EP –, Nov 2015. URL http://dx.doi.org/10.1038/ncomms9913. Article.

[34] Cui-Zu Chang, Jinsong Zhang, Xiao Feng, Jie Shen, Zuocheng Zhang, Minghua Guo, Kang Li, Yunbo Ou, Pang Wei, Li-Li Wang, Zhong-Qing Ji, Yang Feng, Shuaihua Ji, Xi Chen, Jinfeng Jia, Xi Dai, Zhong Fang, Shou-Cheng Zhang, Ke He, Yayu Wang, Li Lu, Xu-Cun Ma, and Qi-Kun Xue. Experimental observation of the quantum anomalous hall effect in a magnetic topological insulator. *Science*, 340(6129): 167–170, 2013. ISSN 0036-8075. doi: 10.1126/science.1234414. URL http://science.sciencemag.org/content/340/6129/167.

[35] Y. S. Hor, P. Roushan, H. Beidenkopf, J. Seo, D. Qu, J. G. Checkelsky, L. A. Wray,

D. Hsieh, Y. Xia, S.-Y. Xu, D. Qian, M. Z. Hasan, N. P. Ong, A. Yazdani, and R. J. Cava. Development of ferromagnetism in the doped topological insulator $bi_{2-x}mn_xte_3$. *Phys. Rev. B*, 81:195203, May 2010. doi: 10.1103/PhysRevB.81.195203. URL `https://link.aps.org/doi/10.1103/PhysRevB.81.195203`.

[36] Jeffrey S. Dyck, Pavel Hájek, Petr Lošt'ák, and Ctirad Uher. Diluted magnetic semiconductors based on $sb_{2-x}v_xte_3$ ($0.01lt$; xlt; 0.03). *Phys. Rev. B*, 65:115212, Mar 2002. doi: 10.1103/PhysRevB.65.115212. URL `https://link.aps.org/doi/10.1103/PhysRevB.65.115212`.

[37] Soo-Whan Kim and Myung-Hwa Jung. Electronic properties of $Gd_xBi_{2-x}Se_3$ single crystals analyzed by Shubnikov-de Haas oscillations. *Applied Physics Letters*, 112 (20):202401, 2018. doi: 10.1063/1.5025654. URL `https://doi.org/10.1063/1.5025654`.

[38] T. Jungwirth, X. Marti, P. Wadley, and J. Wunderlich. Antiferromagnetic spintronics. *Nature Nanotechnology*, 11:231 EP –, Mar 2016. URL `http://dx.doi.org/10.1038/nnano.2016.18`. Review Article.

[39] Y. L. Chen, J.-H. Chu, J. G. Analytis, Z. K. Liu, K. Igarashi, H.-H. Kuo, X. L. Qi, S. K. Mo, R. G. Moore, D. H. Lu, M. Hashimoto, T. Sasagawa, S. C. Zhang, I. R. Fisher, Z. Hussain, and Z. X. Shen. Massive dirac fermion on the surface of a magnetically doped topological insulator. *Science*, 329(5992):659–662, 2010. ISSN 0036-8075. doi: 10.1126/science.1189924. URL `http://science.sciencemag.org/content/329/5992/659`.

[40] Y. R. Song, Fang Yang, Meng-Yu Yao, Fengfeng Zhu, Lin Miao, Jin-Peng Xu, Mei-Xiao Wang, H. Li, X. Yao, Fuhao Ji, S. Qiao, Z. Sun, G. B. Zhang, B. Gao, Canhua Liu, Dong Qian, C. L. Gao, and Jin-Feng Jia. Large magnetic moment of gadolinium substituted topological insulator: Bi1.98gd0.02se3. *Applied Physics*

Letters, 100(24):242403, 2012. doi: 10.1063/1.4729056. URL https://doi.org/10.1063/1.4729056.

[41] T. Valla, Z.-H. Pan, D. Gardner, Y. S. Lee, and S. Chu. Photoemission spectroscopy of magnetic and nonmagnetic impurities on the surface of the bi_2se_3 topological insulator. *Phys. Rev. Lett.*, 108:117601, Mar 2012. doi: 10.1103/PhysRevLett.108.117601. URL https://link.aps.org/doi/10.1103/PhysRevLett.108.117601.

[42] S. W. Kim, S. Vrtnik, J. Dolinek, and M. H. Jung. Antiferromagnetic order induced by gadolinium substitution in bi2se3 single crystals. *Applied Physics Letters*, 106(25): 252401, 2015. doi: 10.1063/1.4922899. URL https://doi.org/10.1063/1.4922899.

[43] Chen Taishi, Liu Wenqing, Zheng Fubao, Gao Ming, Pan Xingchen, van der Laan Gerrit, Wang Xuefeng, Zhang Qinfang, Song Fengqi, Wang Baigeng, Wang Baolin, Xu Yongbing, Wang Guanghou, and Zhang Rong. Highmobility smdoped bi2se3 ferromagnetic topological insulators and robust exchange coupling. *Advanced Materials*, 27(33):4823–4829. doi: 10.1002/adma.201501254. URL https://onlinelibrary.wiley.com/doi/abs/10.1002/adma.201501254.

[44] Bei Deng, Yiou Zhang, S. B. Zhang, Yayu Wang, Ke He, and Junyi Zhu. Realization of stable ferromagnetic order in a topological insulator: Codoping-enhanced magnetism in $4f$ transition metal doped Bi_2Se_3. *Phys. Rev. B*, 94:054113, Aug 2016. doi: 10.1103/PhysRevB.94.054113. URL https://link.aps.org/doi/10.1103/PhysRevB.94.054113.

[45] Bei Deng, Feng Liu, and Junyi Zhu. Absence of quantum anomalous hall state in $4d$ transition-metal-doped Bi_2Se_3: An ab initio study. *Phys. Rev. B*, 96:174404, Nov 2017. doi: 10.1103/PhysRevB.96.174404. URL https://link.aps.org/doi/10.1103/PhysRevB.96.174404.

[46] P. Hohenberg and W. Kohn. Inhomogeneous electron gas. *Phys. Rev.*, 136: B864–B871, Nov 1964. doi: 10.1103/PhysRev.136.B864. URL https://link.aps.org/doi/10.1103/PhysRev.136.B864.

[47] W. Kohn and L. J. Sham. Self-consistent equations including exchange and correlation effects. *Phys. Rev.*, 140:A1133–A1138, Nov 1965. doi: 10.1103/PhysRev.140.A1133. URL https://link.aps.org/doi/10.1103/PhysRev.140.A1133.

[48] P. Blaha, K. Schwarz, G. K. H. Madsen, D. Kvasnicka, and J. Luitz. *WIEN2K, An Augmented Plane Wave + Local Orbitals Program for Calculating Crystal Properties*. Karlheinz Schwarz, Techn. Universität Wien, Austria, 2001.

[49] Chao-Xing Liu, Xiao-Liang Qi, HaiJun Zhang, Xi Dai, Zhong Fang, and Shou-Cheng Zhang. Model hamiltonian for topological insulators. *Phys. Rev. B*, 82:045122, Jul 2010. doi: 10.1103/PhysRevB.82.045122. URL https://link.aps.org/doi/10.1103/PhysRevB.82.045122.

[50] Yongfu Sun, Hao Cheng, Shan Gao, Qinghua Liu, Zhihu Sun, Chong Xiao, Changzheng Wu, Shiqiang Wei, and Yi Xie. Atomically thick bismuth selenide freestanding single layers achieving enhanced thermoelectric energy harvesting. *Journal of the American Chemical Society*, 134(50):20294–20297, 2012. doi: 10.1021/ja3102049. URL https://doi.org/10.1021/ja3102049. PMID: 23214984.

[51] Sungjae Cho, Nicholas P. Butch, Johnpierre Paglione, and Michael S. Fuhrer. Insulating behavior in ultrathin bismuth selenide field effect transistors. *Nano Letters*, 11(5):1925–1927, 2011. doi: 10.1021/nl200017f. URL https://doi.org/10.1021/nl200017f. PMID: 21486055.

[52] V M Garca, M T S Nair, P K Nair, and R A Zingaro. Chemical deposition of bismuth selenide thin films using n,n -dimethylselenourea. *Semiconductor Science*

and Technology, 12(5):645, 1997. URL http://stacks.iop.org/0268-1242/12/i=5/a=020.

[53] Desheng Kong, Jason C. Randel, Hailin Peng, Judy J. Cha, Stefan Meister, Keji Lai, Yulin Chen, Zhi-Xun Shen, Hari C. Manoharan, and Yi Cui. Topological insulator nanowires and nanoribbons. *Nano Letters*, 10(1):329–333, 2010. doi: 10.1021/nl903663a. URL https://doi.org/10.1021/nl903663a. PMID: 20030392.

[54] Yub Raj Sapkota, Asma Alkabsh, Aaron Walber, Hassana Samassekou, and Dipanjan Mazumdar. Optical evidence for blue shift in topological insulator bismuth selenide in the few-layer limit. *Applied Physics Letters*, 110(18):181901, 2017. doi: 10.1063/1.4982631. URL https://doi.org/10.1063/1.4982631.

[55] Xiaoxiong Wang, Peng Wang, Decai Huang, and Weishi Tan. Effects of surface modification on the properties of topological surface states in bi2se3. *Physics Letters A*, 376(5):768 – 772, 2012. ISSN 0375-9601. doi: https://doi.org/10.1016/j.physleta.2011.12.022. URL http://www.sciencedirect.com/science/article/pii/S0375960111014848.

[56] Xiaoxiong Wang and T.-C. Chiang. Topological states in bi_2se_3 surfaces created by cleavage within a quintuple layer: Analysis in terms of the shockley criterion. *Phys. Rev. B*, 89:125109, Mar 2014. doi: 10.1103/PhysRevB.89.125109. URL https://link.aps.org/doi/10.1103/PhysRevB.89.125109.

[57] Andrew S. Hewitt, Jingying Wang, Jon Boltersdorf, Paul A. Maggard, and Daniel B. Dougherty. Coexisting bi and se surface terminations of cleaved bi2se3 single crystals. *Journal of Vacuum Science & Technology B*, 32(4):04E103, 2014. doi: 10.1116/1.4873689. URL https://doi.org/10.1116/1.4873689.

[58] Conor R. Thomas, Matthew K. Vallon, Matthew G. Frith, Hikmet Sezen, Satya K. Kushwaha, Robert J. Cava, Jeffrey Schwartz, and Steven L. Bernasek. Surface

oxidation of bi2(te,se)3 topological insulators depends on cleavage accuracy. *Chemistry of Materials*, 28(1):35–39, 2016. doi: 10.1021/acs.chemmater.5b03923. URL https://doi.org/10.1021/acs.chemmater.5b03923.

[59] Weimin Zhou, Haoshan Zhu, and Jory A. Yarmoff. Termination of single-crystal Bi_2Se_3 surfaces prepared by various methods. *Phys. Rev. B*, 94:195408, Nov 2016. doi: 10.1103/PhysRevB.94.195408. URL https://link.aps.org/doi/10.1103/PhysRevB.94.195408.

[60] John P. Perdew, Kieron Burke, and Matthias Ernzerhof. Generalized gradient approximation made simple. *Phys. Rev. Lett.*, 77:3865–3868, Oct 1996. doi: 10.1103/PhysRevLett.77.3865. URL https://link.aps.org/doi/10.1103/PhysRevLett.77.3865.

VITA

Graduate School
Southern Illinois University

Stephen Hofer

shofer@siu.edu

Southern Illinois University at Carbondale
Bachelor of Science, Physics, May 2010

Thesis Paper Title:
Time Reversal Symmetry Breaking in 4f-doped Topological Insulators

Major Professor: Dr. Dipanjan Mazumdar

Publications:
Recent advances in investigations of the electronic and optoelectronic properties of group III, IV, and V selenide based binary layered compounds, J. Mater. Chem. C, 2017,5, 11214-11225